Affinity-ranking BIN1 interactions and screening natural BIN1 variants that may cause neuromuscular disorders

Boglarka Zambo[1], Evelina Edelweiss[2], Bastien Morlet[2], Luc Negroni[2], Soren Ostergaard[3], Jocelyn Laporte[2*], Gilles Trave[1*], Gergo Gogl[1*]

[1] Equipe Labellisee Ligue 2015, Departement de Biologie Structurale Integrative, Institut de Genetique et de Biologie Moleculaire et Cellulaire (IGBMC), INSERM U1258/CNRS UMR 7104/Universite de Strasbourg, 1 rue Laurent Fries, BP 10142, F-67404 Illkirch, France
[2] Institut de Genetique et de Biologie Moléculaire et Cellulaire (IGBMC), INSERM U1258/CNRS UMR 7104/Université de Strasbourg, 1 rue Laurent Fries, BP 10142, F-67404 Illkirch, France
[3] Novo Nordisk A/S, Global Research Technologies, Novo Nordisk Research Park, 2760 Maaloev, Denmark
*co-corresponding authors: goglg@igbmc.fr, jocelyn@igbmc.fr, travegi@igbmc.fr

Abstract

Deletion of the protein-protein interaction SH3 domain of the membrane remodeling BIN1 protein was found to lead to centronuclear myopathy in patients, yet only few interaction partners of BIN1 SH3 have been identified so far. Here we used the holdup assay to proteome-wide measure steady-state affinity constants of BIN1 SH3 domain for thousands of full-length cellular proteins, as well as for hundreds of putative SH3-binding sites found within the identified BIN1 binders. Besides confirming known partners, such as DNM2, we also identified and affinity-characterized numerous others. We also assessed the impact of a set of rare natural BIN1 SH3 domain variants on affinity interactomes and identified a set of potentially harmful ones that exhibited perturbed affinity profiles, whose impacts were confirmed by cellular assay, tentatively connecting them to neuromuscular disorders.

Introduction

Bridging Integrator 1 (BIN1), also known as Amphiphysin 2 (AMPH2), is a ubiquitously expressed adaptor protein involved in membrane remodeling. It contains an N-terminal BAR domain required for membrane binding — named after BIN1, AMPH, and RVS167 — and a C-terminal SRC Homology 3 (SH3) domain, required for partner recruitment (Prokic *et al*, 2014) (Peter *et al*, 2004) (Owen *et al*, 1998). BAR domain deposition on membrane surfaces causes membrane curvature and BIN1-mediated membrane remodeling was found to be critical in the formation of various endomembrane structures, such as clathrin or caveolin coated vesicles, recycling endosomes, as well as tubular invaginations of the plasma membrane in muscle cells, known as T-tubules (Lee *et al*, 2002) (Razzaq *et al*, 2001) (Ramjaun & McPherson, 1998). Besides membrane remodeling, a well-studied function of BIN1 is to recruit Dynamin 2 (DNM2) to curved membranes, whose local oligomerization appears to be critical in both membrane fission during vesicle scission and in the formation of T-tubules in muscle cells (Cowling *et al*, 2017) (David *et al*, 1996) (Volchuk *et al*, 1998) (Figure 1A). Both BIN1 and DNM2 are implicated in centronuclear myopathy (CNM): mutations of DNM2 were found to lead to autosomal dominant CNM and mutations of BIN1 were found to lead to autosomal recessive CNM (Bitoun *et al*, 2005) (Nicot *et al*, 2007) (Gómez-Oca *et al*, 2022). Disease-associated mutations of BIN1 can occur at several positions. Those BIN1 mutations that are located in its BAR domain prevent its membrane remodeling function, resulting in the nearly complete loss of BIN1-related cellular mechanisms (Nicot *et al*, 2007). Importantly, rarely occurring truncations of the SH3 domain of BIN1 (caused by early stop codons such as Q573*, or K575*) also result in CNM (Nicot *et al*, 2007) (Laiman *et al*, 2023). These BIN1 variants are still capable to participate in membrane remodeling because their BAR domains are

unaffected, but they are unable to anchor partner proteins, like DNM2, to the curved membranes. In addition, a frameshift mutation causing a mostly hydrophobic 52-residue extension of the BIN1 SH3 domain was found to cause autosomal dominant CNM (Böhm *et al*, 2014). These observations indicate the critical role of the SH3 domain of BIN1 and its mediated protein-protein interactions in CNM. At last, molecular characterization of the SH3 domain-mediated interactions of BIN1 and their molecular functions are of particular importance, as exogenous expression of BIN1 is a promising therapeutic approach to treat CNM (Lionello *et al*, 2022) (Lionello *et al*, 2019).

SH3 domains recognize Proline-rich motifs (PRMs), most typically basic PxxP motifs (Lim *et al*, 1994) (Figure 1B). DNM2 contains an extensive Proline-rich region (PRR) in its C-terminal tail including a series of putative PRMs that is thought to interact with the SH3 domain of BIN1 (Grabs *et al*, 1997). Consequently, the widely accepted view is that disruption of cellular BIN1-DNM2 complex leads to CNM. However, SH3 domains are typically highly promiscuous and can bind to hundreds of partners, similarly to other protein-protein interaction domain families (Wu *et al*, 2007) (Gogl *et al*, 2022). Therefore, it is likely that mutations disrupting the BIN1 SH3 domain will also affect BIN1 binding to other partners than DNM2 and that these effects will contribute collectively to the disease development. However, only a handful of SH3-mediated interactions of BIN1 were identified besides DNM2 until now, such as MYC, TAU, RIN3, and Caveolae-associated protein 4 (CAVIN4) (Andresen *et al*, 2012) (Pineda-Lucena *et al*, 2005) (Lasorsa *et al*, 2018) (Malki *et al*, 2017) (Kajiho *et al*, 2003) (Lo *et al*, 2021). Viral proteins were also found to interact with the BIN1 SH3 domain (Nanda *et al*, 2006) (Tossavainen *et al*, 2016). Besides these sparse interactions of the BIN1 SH3 domain that were found with low-throughput approaches, the interactome of full-length (FL) BIN1 was screened in multiple high-throughput interactomic studies (Ellis *et al*, 2012) (Luck *et al*, 2020) (Huttlin *et al*, 2021) (Cho *et al*, 2022), but the resulting BIN1 interactomes overlapped poorly (Figure 1C). These observations suggested that BIN1 had a limited set of interaction partners, which implied that its SH3 domain, did not have a promiscuous interactomic nature unlike other SH3 domains.

Here, we attempt to chart an unbiased affinity interactomic map of the SH3 domain of BIN1 using a top-down quantitative interactomic strategy — exploiting full advantages of our recently developed experimental approaches — to unveil widespread molecular interactions of BIN1 that are likely disrupted in CNM. We first investigated the binding of BIN1 to nearly 7,000 FL proteins from cell extracts, out of which we quantified apparent dissociations constants for ca. 200 interaction partners, typically in the low-micromolar dissociation constant regime. Then, we identified and synthetized all putative PRMs found in their sequence (448 PxxP motifs) and systematically measured their binding affinities with the SH3 domain of BIN1 in order to reveal the site-specific molecular driving forces between BIN1 and its target proteins. Finally, we compared affinity interactomes of previously uncharacterized rare naturally occurring BIN1 variants to assess their impact on biophysical binding properties in order to identify variants with possible pathological impacts.

Results

Deciphering the intrinsic affinity interactome of the SH3 domain of BIN1 using native holdup

The holdup assay is an established method to quantify equilibrium binding constants between resin-immobilized bait and in-solution analyte molecules (Charbonnier *et al*, 2006) (Vincentelli *et al*, 2015) (Gogl *et al*, 2022). The main advantage of holdup over

conventional pulldown-based approaches is that it captures the undisturbed binding equilibrium by quantifying the relative amount of unbound preys in the supernatant, instead of measuring the enrichment of bound prey on the resin after washing steps (Charbonnier *et al*, 2006). These measured relative prey concentrations, often referred to as binding intensities (BI), can be converted to equilibrium dissociation constants (Vincentelli *et al*, 2015) (Gógl *et al*, 2019) (Gogl *et al*, 2020) (Delalande *et al*, 2022). A recent variation of the method, called native holdup (nHU), uses dilute cell extracts as analyte, providing estimates of equilibrium dissociation constants for thousands of full-length endogenous proteins from a single experiment (Zambo *et al*, 2022). We used this approach to estimate the steady-state dissociation constants of the complexes formed between the BIN1 SH3 domain (BIN1_SH3) and all detectable FL protein from total Jurkat extracts. We performed single-point nHU experiments at 10 μM estimated bait concentration, quantified the prey depletion with label-free quantitative mass spectrometry (MS), and converted the obtained BI values to apparent equilibrium binding affinities using a simple bimolecular binding model (hyperbolic formula) (Figure 2, Table S1). With this experimental setup, we assayed the binding of 6,357 FL proteins, out of which 188 showed statistically significant binding to BIN1_SH3 displaying dissociation constants in the range of 0.5-34 μM.

We also included 5 other SH3 domains in the same experiment series, taken from Amphysisin (AMPH), Abelson murine leukemia viral oncogene homolog 1 (ABL1), Rho guanine nucleotide exchange factor 7 (ARHGEF7), Protein arginine N-methyltransferase 2 (PRMT2), and Obscurin (OBSCN). These other SH3 domains showed comparable promiscuity with BIN1 with the exception of OBSNC_SH3, whose interactome appears to be markedly less promiscuous with only a few detected interaction partners (Figure S1, Table S1). For these domains, we quantified pairwise interactomic similarities with BIN1_SH3 using the affinities of interaction partners that showed binding to both SH3 domains (Figure 2, Figure S1, Table S1). We have found that the affinity profiles of AMPH_SH3 and ARHGEF7_SH3 show statistically significant correlation with the affinity profile of BIN1_SH3, albeit their shared substrates display non-identical affinities. In contrast, the affinities of the shared substrates between BIN1 and ABL1_SH3 or PRMT2_SH3 differ substantially with no significant correlation.

We also performed an independent nHU experiment with the BIN1_SH3 bait under identical conditions and quantified prey depletion using a different mass spectrometer to further validate the obtained affinity interactome of BIN1, as well as to further expand the list of screened preys and to identify more interaction partners. Between the affinities of the partners that we identified in both experiments, a strong proportionality was found with statistical significance (Figure S1F). By combining the results of the two experiment series, we assayed the binding of 6,453 FL endogenous proteins, out of which 206 showed significant binding to BIN1.

Analyzing the interaction partners of BIN1

Identified interaction partners can be ranked in the context of the unbiased affinity-interactomic profile of the BIN1 SH3 domain based on their apparent affinity constants derived from the nHU assay (Figure 3A). Among the significant BIN1_SH3 binders detected by our assay, three proteins were previously found to bind FL BIN1 in high-throughput qualitative interactomic studies: DNM2, ITCH, and SMCHD1. These interaction partners were found to rank among the strongest interaction partners of BIN1_SH3. Eight proteins (ATXN2, DNM2, DNMT1, MORC2, MTPAP, SBF1, SMCHD1, SPAST) are encoded by genes which, like BIN1 itself, are listed in a previously assembled gene table of monogenic neuromuscular disorders (Cohen *et al*, 2021). Another significant BIN1_SH3 binder detected by our assay is MTMR1, a close paralog of myotubularin (MTM1) whose

mutation can cause the X-linked form of CNM also called myotubular myopathy (Zanoteli *et al*, 2005). Five out of these phenotypically-related partners (DNM2, SMCHD1, DNMT1, MORC2, and SBF1) were found to display relatively high affinity with BIN1_SH3 with a dissociation constant < 10 μM (pK_d > 5), while ATXN2, SPAST, MTMR1, and MTPAP showed somewhat weaker affinities. Out of these, DNMT1, SPAST, and MTPAP only showed detectable binding to BIN1_SH3, while SMCHD1, MORC2, and MTMR1 also showed detectable binding to the SH3 domains of AMPH (Table S1). The remaining partners (DNM2, SBF1, ATXN2, ITCH) were found to be more promiscuous, displaying affinities with the SH3 domains of BIN1, AMPH, as well as other proteins involved in our screens.

Single-point nHU experiments are highly efficient to identify interaction partners and to provide estimations for their dissociation constants, but they have their limitations (Zambo *et al*, 2022). For example, if cooperativity or partial activity occurs, apparent affinities can over or underestimate the real affinities. As the interaction between BIN1 and DNM2 is of particular clinical importance and because it was found to rank among the strongest interactions of BIN1, we also performed a complementary nHU titration experiment using myoblast extracts that eliminates several limitations of the single-point experiments (Figure 3B, Figure S2A). We have found that DNM2 displays a partial binding activity with only ca. 76% binding capable fraction, but binds to BIN1 with high affinity with a dissociation constant of 50 nM (pK_d = 7.3), making DNM2 the strongest BIN1_SH3 partner displaying the highest obtained steady-state affinity (Figure 3). To further investigate the binding mechanisms of the DNM2-BIN1 interaction, we performed a holdup experiment with catalytically active recombinant DNM2, purified from insect cells, as prey and BIN1_SH3 as a bait, under identical conditions to the previous nHU experiment (Figure 3C, Figure S2B, S3). We found that purified recombinant DNM2 interacts with the BIN1 SH3 domain with similar affinity to that obtained for endogenous DNM2 directly from myoblast extract, also displaying similar apparent partial binding activity. Apparent partial binding can occur for many reasons, such as due to prey heterogeneity or due to technical artifacts, as discussed in great details in the method section.

Deciphering the site-specific affinity interactome of BIN1 using fragmentomic holdup

PRMs are extremely common in our proteome. For example, only considering the two most common types of PxxP motifs, we could identify more than 10,000 motifs within ca. 5,000 proteins in the ca. 20,000 proteins encoded in our genome (Kumar *et al*, 2019) (Krystkowiak & Davey, 2017). Therefore, it is expected that 25% of the identified interaction partners of BIN1 will contain PRMs, even by chance. However, we have found putative PRMs in 65% of the interaction partners of BIN1 (133 out of 206), indicating a large >2.5-fold enrichment compared to the random occurrence (Figure 2, Table S1). Within disordered regions of these proteins, we identified 417 putative PRMs matching the [RK]..P..P or P..P.[RK] consensus motifs (class 1 and class 2 PxxP motifs, respectively). We also identified 31 PRMs found in 19 potential interaction partners of BIN1 that showed ambiguous binding in the nHU experiments (strong binding with low statistical significance). All these 448 putative PRMs were synthesized as 15-mer biotinylated peptides to use them as baits in our recently developed ultra-high-throughput fragmentomic holdup assay (Gogl *et al*, 2022). This assay relies on the same principle as native holdup, but uses biotinylated peptides as baits and purified proteins (His_6-MBP-fused SH3 domains) as preys and measures prey depletion by intrinsic fluorescence.

With this assay, we have found 176 motifs that showed detectable binding with BIN1 (Figure 4A, Table S2). These motifs were originating from 97 FL proteins, out of

which only 5 showed ambiguous binding in nHU. Therefore, out of 133 interaction partners of BIN1_SH3 that contain putative PRMs, we matched 92 with at least one quantified site-specific affinity, annotating nearly half of all identified BIN1_SH3 partners with detailed biophysical measurements. The remaining, not yet annotated interaction partners of BIN1 may interact indirectly, or via other types of PRMs that were not screened in our assay. Although the nHU assay is highly powerful to identify transient interactions from cell extracts and to characterize their intrinsic binding properties, it does not indicate which part of the identified partner is responsible for the interaction. Complementing it with the fragmentomic holdup approach, we could identify the sites that contribute to the interactions (Figure 4B). For example, SMCHD1 mediates a high affinity interaction with BIN1_SH3, but it contains 3 putative binding sites. Out of these, two turned out to be unable to bind BIN1_SH3 above detection in the fragmentomic assay, while the third peptide fragment mediates similarly strong affinity with BIN1_SH3 as FL SMCHD1. Some proteins contained more than one putative PRM that bound BIN1_SH3 above detection. For example, instead of finding a single peptide that detectably interacts out of the many, we identified several PRMs in the PRR of DNM2 that displayed weak affinities in isolation but presumably could establish high-affinity binding through cooperation and synergy, as well as oligomerization of the FL protein.

By comparing the PRM-binding affinities of the SH3 domain of BIN1 with the corresponding affinities of the 5 other SH3 domains addressed in our study, we have found good agreement with the biophysical similarities previously observed with FL partner binding (Figure S4, Table S2). Similarly to the previous experiments, the affinity profile of BIN1_SH3 was most similar to the affinity profile of AMPH_SH3, and was also similar to the affinity profile of ARHGEF7_SH3, but was more distinct from the affinity profiles of PRMT2_SH3 or ABL1_SH3. In addition, the SH3 domain of OBSCN was found to only mediate detectable binding to a handful of PRMs included in our panel signifying its peculiar nature compared to the other SH3 domains. These similarities and differences in the binding preferences could be explained by calculating affinity-weighted specificity logos based on the PRM-binding affinity profiles that can help to understand the sequence requirements of forming high-affinity interactions (Figure 4C, S4). We have found that BIN1_SH3 has a clear preference for class 2 PxxP motifs over class 1 motifs, similarly to the SH3 domains of AMPH and ARHGEF7. In contrast, PRMT2_SH3 does not appear to have a marked specificity and both ABL1_SH3 and OBSCN_SH3 appears to prefer class 1 PxxP motifs. Therefore, we have found that the SH3 domains of BIN1, AMPH, and ARHGEF7 have similar binding preferences to class 2 PxxP motifs, resulting in similar affinity interactomes against both PRM fragments, and FL partner proteins. In contrast, the SH3 domains of ABL1, PRMT2, and OBSCN have preferences for other kinds of PRMs, making their affinity interactomes distinct from the affinity interactome of the BIN1 SH3 domain.

The impact of missense variants on the affinity interactome and cellular function of BIN1

Modern genomics provides an invaluably rich resource for finding naturally occurring sequence variants of proteins, yet the clinical significance of most are uncertain (Sherry *et al*, 2001) (Landrum *et al*, 2020) (Karczewski *et al*, 2020). Although modern structure-prediction tools are capable to investigate the structural consequences of these mutations, current algorithms are not yet capable to foresee the large-scale consequences on their functions, especially if these effects are mild (Tunyasuvunakool *et al*, 2021) (Fu *et al*, 2022). One of the major goals of interactomics is to allow functional description for these observed variants, yet interactomics mostly relies on qualitative tools (Sahni *et al*, 2015). Here, we attempt to quantitatively compare affinity interactomes of naturally occurring

protein variants using our fragmentomic holdup assay. We selected 1 common, likely benign, and 8 rare variants, with unknown clinical significance, of the BIN1 SH3 domain to characterize their PRM-binding affinity interactomes using our previously established library of 448 PRM peptides (Figure 5A).

We selected sequence variations that either occur near the PxxP binding cleft of the SH3 domain, or that may cause indirect effect on the interactome of the SH3 domain by changing either the domain folding or domain stability (Figure 5B). 4 mutations (Y531S, T532M, D537V, and Q540H) are situated on the RT loop, P551L can be found on the n-Src loop, while V566M, V83I, and F584S are integral part of the β-strands of the SH3 fold. After measuring the affinity interactomes of these variants, we compared them to the affinity profile of wild type (WT) BIN1_SH3 by calculating cumulative Euclidean affinity distances (Figure 5A, C, Figure S5, Table S2). (Note that the resulting ΔpK_d is proportional to $\Delta\Delta G$.) We found that only 3 variants caused substantial perturbation in the affinity interactome. The mutations Y531S, D537V are placed on the RT loop and are integral part of the PRM binding interface and they cause perturbed affinity profiles (PAP) where a general affinity interactome reshuffling was observed where most peptide targets mediate weaker affinities compared to the WT SH3 domain. In contrast, the mutation F584S causes a near complete loss of function (LOF) of the BIN1 SH3 domain. This residue is placed on the β4-strand facing the hydrophobic core and the mutation likely causes a destabilized SH3 fold. Besides, based on the very similar interactomic properties of the other variants to WT BIN1, it is likely that these are benign variants. In support of this, the common variant T532M, that displays affinity interactome quasi identical to WT BIN1, is present 116 times at homozygous state in genomic databases with no connection to any clinical phenotype (Karczewski *et al*, 2020).

In a previous study, point mutations were used to map the DNM2 binding interface on BIN1 and two of their mutations coincide with the natural variants displaying perturbed affinity interactomes (Owen *et al*, 1998). Similarly to our findings with Y531S and D537V, the authors found Y531F and D537A variants to cause a marked loss of DNM2 binding activity. Since the binding of DNM2 is highly synergistic between many weak PRMs, we also measured the binding of a larger section of the DNM2 PRR (residues 823-860) against all tested BIN1 variants (Figure 6A). We have found that this region was displaying larger affinity than any of the isolated PRM found within its sequence, yet its binding affinity was still much weaker than the affinity of FL DNM2, indicating a possible important contribution of DNM2 oligomers in mediating high-affinity binding to SH3 domains. Regardless, these experiments confirmed that the three studied variants (Y531S, D537V, F584S) are unable to detectably interact with the PRR of DNM2 while the other variants display very similar affinities as WT BIN1.

At last, we tested whether the natural variants impacting the affinity interactome of BIN1 are capable to recruit DNM2 to BIN1-induced membrane invaginations. We co-transfected Cos-1 cells with GFP-BIN1 (FL, isoform 8) and Myc-DNM2 (FL) as described previously (Lionello *et al*, 2022) (Figure 6B-C, Figure S6). We performed membrane tubulation assay with WT BIN1, with the likely benign Q540H variant, as well as with the three variants that displayed perturbed affinity interactomes. As expected, all tested BIN1 variants were capable to promote tubular endomembrane structures, since this process is mediated by the BAR domain of BIN1 and not by its SH3 domain. Furthermore, the WT and the likely benign Q540H variant were capable to efficiently anchor DNM2 to these foci. Unexpectedly, the F584S variant, that showed a nearly completed LOF in the interactomic screen, could also recruit DNM2, however, the tubules formed by this variant appeared to be less polarized and organized than the WT. The Y531S and D537V variants, that

localizes at the interface between the two proteins, were showed markedly reduced ability to recruit DNM2, confirming our interactomic results. Based on these observations, we think that the SH3 domain of BIN1 is somewhat destabilized in isolation whereas it is stabilized by interactions with other regions of the full-length protein (Kojima *et al*, 2004) (Wu & Baumgart, 2014). As a consequence, the destabilizing F584S SH3 domain variant could be rescued in the context of the FL BIN1 protein, while the other variants affecting the binding interface of the SH3 domain itself are not possible to rescue. Thus, we confirmed the impact of the interactomic perturbation in a cellular context, since all the three variants with identified affinity-interactomic impact displayed an altered cellular phenotype in the tubulation assay, implying a potential clinical significance that should be further validated for these rare variants.

Discussion

Here, we developed an innovative top-down quantitative interactomic strategy that combines two state-of-the-art holdup-based methods developed by our team. Interactions mediated by short linear motifs are most often highly transient and routinely used interactomic techniques often fail to detect them (Kassa *et al*, 2023). Our new strategy was found to be particularly powerful to identify and characterize these interactions. The unbiased nHU approach could both identify interactions including these transient ones and characterize their apparent intrinsic properties at the same time, yet it could not decipher site-specific biophysical processes. The fragmentomic holdup approach is suitable to map these site-specific events by measuring interactions between synthetic peptides and purified domains, although relying only on this approach could require the screening a huge number of putative motifs to find the ones that could bind with high affinity to a given protein of interest. Taken the combination of these two methods by using nHU as a guide for fragmentomic measurement, our strategy provides the most advanced way to get insight into the formation of transient complexes.

As introduced above, previously only a handful of BIN1 interaction partners were known. With the help of our quantitative interactomic approach, by only focusing on its SH3 protein-protein interaction domain, we described more than 200 FL interaction partners of the SH3 domain of BIN1 and we have found functional BIN1-binding sites within half of them using the fragmentomic holdup approach. From these experiments, we concluded that DNM2 indeed interacts with BIN1 with very high affinity through a stretch of suboptimal PxxP motifs in its C-terminal PRR. Individually, these motifs bind relatively weak, however when combined, they form much stronger interactions, which is likely also reinforced by the oligomerization of DNM2. Noteworthy, mutations in BIN1 or DNM2 lead to different forms of CNM. Although DNM2 ranks among the highest affinity interactions of BIN1, signifying the importance of this interaction, we also identified many other interaction partners with similar affinities that may be also critical for understanding the cellular activities of BIN1, as well as the phenotypes linked to BIN1 mutations. For example, we identified SMCHD1 as a strong interaction partner and identified that it interacts with BIN1 through an optimal C-terminal class 2 PxxP motif that displays similar affinity to BIN1 as full-length SMCHD1. Interestingly, mutations of this protein also leads to a neuromuscular disorder called facioscapulohumeral muscular dystrophy (FSHD) and both FSHD and CNM patients suffer from muscle weakness as a major symptom. Our systematic unbiased study suggests that this complex may play a role in the symptomatic manifestations of both conditions. Nevertheless, disruptive mutations in the SH3 domain of BIN1 affect all identified interactions, and even if they display weak affinities, the loss of these interactions collectively contributes to CNM.

Rare variants of uncertain clinical significance are a major challenge in interpreting genetic results. Only considering the very short SH3 domain of BIN1, we could identify dozens of sequence variations in genomic databases out of which nearly none were studied with functional assays previously. To shed light on the potential importance of these rare variants, we systematically screened affinity interactomes of a panel of naturally occurring missense variants of uncertain clinical significance. While we found that most of these variants do not cause detectable perturbation in the intrinsic affinity interactome of BIN1, we identified 3 rare variants that caused affinity rewiring, leading to altered cellular phenotypes related to BIN1. Although these variants were only found in a few individuals in high-throughput genomic screens, who may represent healthy heterozygous carriers of the mutation, and therefore there is no statistical evidence for causality between genotype and pathology, our quantitative interactomic screen has associated them with putative clinical risk. In conclusion, we demonstrated that quantitative interactomics is not limited to search and characterize interaction partners, but also suitable for testing effects of sequence variations in order to identify potentially disease-causing mutations.

Acknowledgment
We thank Pascal Eberling for the synthesis of the DNM2 PRR peptide, Camille Kostmann for help in cloning, Nadege Diedhiou for her help in the tubulation assay, as well as the cell culture and the photonic microscopy platform of the IGBMC for their help in cell culturing and imaging. GG was supported by the collaborative post-doc grant of IGBMC. The project was supported by the Ligue contre le cancer (équipe labellisée 2015 to GT), the Agence Nationale de la Recherche (grant ANR-18-CE92-0017, ANR-22-CE44-0018, and ANR-22-CE11-0026 to GT). As a member of the IGBMC institute, we benefited from the French Infrastructure for Integrated Structural Biology (FRISBI) ANR-10-INSB-05-01, from Instruct-ERIC, from IdEx Unistra (ANR-10-IDEX-0002), from SFRI-STRAT'US project (ANR 20-SFRI-0012), and from EUR IMCBio (ANR-17-EURE-0023) under the framework of the French Investments for the Future Program as a member of the Interdisciplinary Thematic Institute IMCBio, as part of the ITI 2021-2028 program of the University of Strasbourg, CNRS and Inserm.

Author contribution
All nHU and HU experiments and data analysis, cloning and expression of SH3 domains were performed by BZ and GG. BZ performed all WB and tubulation assays. MS experiments and primary data analysis were performed by BM and LN. Peptide arrays were prepared by SO. EE prepared recombinant DNM2 and grew the myoblast cells. BZ grew the Jurkat cells and prepared the cell extracts. GG, JL, and GT conceived and supervised the project. GG wrote the paper and all authors reviewed the manuscript.

Conflict of Interest
The authors declare that they have no competing interests.

Data and materials availability
All data needed to evaluate the conclusions in the paper are present in the paper, in the Supplementary Materials and in public databases. Raw mass spectrometry data are available in the PRIDE database with identifiers 1-20230214-20023.

References

Andresen C, Helander S, Lemak A, Farès C, Csizmok V, Carlsson J, Penn LZ, Forman-Kay JD, Arrowsmith CH, Lundström P, *et al* (2012) Transient structure and dynamics

in the disordered c-Myc transactivation domain affect Bin1 binding. *Nucleic Acids Res* 40: 6353–6366

Bitoun M, Maugenre S, Jeannet PY, Lacène E, Ferrer X, Laforêt P, Martin JJ, Laporte J, Lochmüller H, Beggs AH, *et al* (2005) Mutations in dynamin 2 cause dominant centronuclear myopathy. *Nat Genet* 37: 1207–1209

Böhm J, Biancalana V, Malfatti E, Dondaine N, Koch C, Vasli N, Kress W, Strittmatter M, Taratuto AL, Gonorazky H, *et al* (2014) Adult-onset autosomal dominant centronuclear myopathy due to BIN1 mutations. *Brain* 137: 3160–3170

Charbonnier S, Zanier K, Masson M & Travé G (2006) Capturing protein-protein complexes at equilibrium: The holdup comparative chromatographic retention assay. *Protein Expr Purif* 50: 89–101

Cho NH, Cheveralls KC, Brunner A-D, Kim K, Michaelis AC, Raghavan P, Kobayashi H, Savy L, Li JY, Canaj H, *et al* (2022) OpenCell: Endogenous tagging for the cartography of human cellular organization. *Science (80-)* 375

Cohen E, Bonne G, Rivier F & Hamroun D (2021) The 2022 version of the gene table of neuromuscular disorders (nuclear genome). *Neuromuscul Disord* 31: 1313–1357

Cowling BS, Prokic I, Tasfaout H, Rabai A, Humbert F, Rinaldi B, Nicot AS, Kretz C, Friant S, Roux A, *et al* (2017) Amphiphysin (BIN1) negatively regulates dynamin 2 for normal muscle maturation. *J Clin Invest* 127: 4477–4487

David C, McPherson PS, Mundigl O & De Camilli P (1996) A role of amphiphysin in synaptic vesicle endocytosis suggested by its binding to dynamin in nerve terminals. *Proc Natl Acad Sci U S A* 93: 331–335

Delalande F, Gogl G, Rohrbacher A, Kostmann C, Eberling P, Carapito C, Travé G & Monsellier E (2022) The Holdup Multiplex , an assay for high-throughput measurement of protein- ligand affinity constants using a mass-spectrometry readout. *bioRxiv*: 1–36

Ellis JD, Barrios-Rodiles M, Çolak R, Irimia M, Kim TH, Calarco JA, Wang X, Pan Q, O'Hanlon D, Kim PM, *et al* (2012) Tissue-Specific Alternative Splicing Remodels Protein-Protein Interaction Networks. *Mol Cell* 46: 884–892

Fu X, Reglero C, Swamy V, Loh JW, Khiabanian H, Albero R, Forouhar F, Alquraishi M, Ferrando AA, Rabadan R, *et al* (2022) Computational structure prediction methods enable the systematic identification of oncogenic mutations. *bioRxiv*

Gógl G, Biri-Kovács B, Durbesson F, Jane P, Nomine Y, Kostmann C, Bilics V, Simon M, Reményi A, Vincentelli R, *et al* (2019) Rewiring of RSK–PDZ Interactome by Linear Motif Phosphorylation. *J Mol Biol* 431: 1234–1249

Gogl G, Jane P, Caillet-Saguy C, Kostmann C, Bich G, Cousido-Siah A, Nyitray L, Vincentelli R, Wolff N, Nomine Y, *et al* (2020) Dual Specificity PDZ- and 14-3-3-Binding Motifs: A Structural and Interactomics Study. *Structure* 28: 747-759.e3

Gogl G, Zambo B, Kostmann C, Cousido-Siah A, Morlet B, Durbesson F, Negroni L, Eberling P, Jane P, Nomine Y, *et al* (2022) Quantitative fragmentomics allow affinity mapping of interactomes. *Nat Commun* 13: 1–18

Gómez-Oca R, Edelweiss E, Djeddi S, Gerbier M, Massana-Muñoz X, Oulad-Abdelghani M, Crucifix C, Spiegelhalter C, Messaddeq N, Poussin-Courmontagne P, *et al* (2022) Differential impact of ubiquitous and muscle dynamin 2 isoforms in muscle physiology and centronuclear myopathy. *Nat Commun* 13: 1–20

Grabs D, Slepnev VI, Songyang Z, David C, Lynch M, Cantley LC & De Camilli P (1997) The SH3 domain of amphiphysin binds the proline-rich domain of dynamin at a single site that defines a new SH3 binding consensus sequence. *J Biol Chem* 272: 13419–13425

Huttlin EL, Bruckner RJ, Navarrete-Perea J, Cannon JR, Baltier K, Gebreab F, Gygi MP, Thornock A, Zarraga G, Tam S, *et al* (2021) Dual proteome-scale networks reveal cell-specific remodeling of the human interactome. *Cell* 184: 3022-3040.e28

Kajiho H, Saito K, Tsujita K, Kontani K, Araki Y, Kurosu H & Katada T (2003) RIN3: A novel Rab5 GEF interacting with amphiphysin II involved in the early endocytic pathway. *J Cell Sci* 116: 4159–4168

Karczewski KJ, Francioli LC, Tiao G, Cummings BB, Alföldi J, Wang Q, Collins RL, Laricchia KM, Ganna A, Birnbaum DP, *et al* (2020) The mutational constraint spectrum quantified from variation in 141,456 humans. *Nature* 581: 434–443

Kassa E, Jamshidi S, Mihalič F, Simonetti L, Kliche J, Jemth P, Sara Bergström Lind & Ivarsson Y (2023) Evaluation of affinity-purification coupled to mass spectrometry approaches for capture of short linear motif-based interactions. *Anal Biochem* 663

Kojima C, Hashimoto A, Yabuta I, Hirose M, Hashimoto S, Kanaho Y, Sumimoto H, Ikegami T & Sabe H (2004) Regulation of Bin1 SH3 domain binding by phosphoinositides. *EMBO J* 23: 4413–4422

Krystkowiak I & Davey NE (2017) SLiMSearch: A framework for proteome-wide discovery and annotation of functional modules in intrinsically disordered regions. *Nucleic Acids Res* 45: W464–W469

Kumar M, Gouw M, Michael S, Sámano-Sánchez H, Pancsa R, Glavina J, Diakogianni A, Valverde JA, Bukirova D, Čalyševa J, *et al* (2019) ELM—the eukaryotic linear motif resource in 2020. *Nucleic Acids Res* 48: 1–11

Laiman J, Hsu YJ, Loh J, Tang WC, Chuang MC, Liu HK, Yang WS, Chen BC, Chuang LM, Chang YC, *et al* (2023) GSK3α phosphorylates dynamin-2 to promote GLUT4 endocytosis in muscle cells. *J Cell Biol* 222

Landrum MJ, Chitipiralla S, Brown GR, Chen C, Gu B, Hart J, Hoffman D, Jang W, Kaur K, Liu C, *et al* (2020) ClinVar: Improvements to accessing data. *Nucleic Acids Res* 48: D835–D844

Lasorsa A, Malki I, Cantrelle FX, Merzougui H, Boll E, Lambert JC & Landrieu I (2018) Structural basis of tau interaction with BIN1 and regulation by tau phosphorylation. *Front Mol Neurosci* 11: 1–12

Lee E, Marcucci M, Daniell L, Pypaert M, Weisz OA, Ochoa GC, Farsad K, Wenk MR & De Camilli P (2002) Amphiphysin 2 (Bin1) and T-tubule biogenesis in muscle. *Science (80-)* 297: 1193–1196

Lim WA, Richards FM & Fox R (1994) Structural determinants of peptide-binding orientation and of sequence specificity in SH3 domains. *Nature* 372: 375–379

Lionello VM, Kretz C, Edelweiss E, Crucifix C, Gómez-Oca R, Messaddeq N, Buono S, Koebel P, Muñoz XM, Diedhiou N, *et al* (2022) BIN1 modulation in vivo rescues dynamin-related myopathy. *Proc Natl Acad Sci U S A* 119

Lionello VM, Nicot AS, Sartori M, Kretz C, Kessler P, Buono S, Djerroud S, Messaddeq N, Koebel P, Prokic I, *et al* (2019) Amphiphysin 2 modulation rescues myotubular myopathy and prevents focal adhesion defects in mice. *Sci Transl Med* 11

Lo HP, Lim YW, Xiong Z, Martel N, Ferguson C, Ariotti N, Giacomotto J, Rae J, Floetenmeyer M, Moradi SV, *et al* (2021) Cavin4 interacts with bin1 to promote t-tubule formation and stability in developing skeletal muscle. *J Cell Biol* 220

Luck K, Kim DK, Lambourne L, Spirohn K, Begg BE, Bian W, Brignall R, Cafarelli T, Campos-Laborie FJ, Charloteaux B, *et al* (2020) A reference map of the human binary protein interactome. *Nature* 580: 402–408

Malki I, Cantrelle FX, Sottejeau Y, Lippens G, Lambert JC & Landrieu I (2017) Regulation of the interaction between the neuronal BIN1 isoform 1 and Tau proteins – role of the SH3 domain. *FEBS J* 284: 3218–3229

Nanda SK, Herion D & Liang TJ (2006) The SH3 binding motif of HCV NS5A protein interacts with Bin1 and is important for apoptosis and infectivity. *Gastroenterology* 130: 794–809

Nicot AS, Toussaint A, Tosch V, Kretz C, Wallgren-Pettersson C, Iwarsson E, Kingston H, Garnier JM, Biancalana V, Oldfors A, *et al* (2007) Mutations in amphiphysin 2 (BIN1) disrupt interaction with dynamin 2 and cause autosomal recessive centronuclear myopathy. *Nat Genet* 39: 1134–1139

Owen DJ, Wigge P, Vallis Y, Moore JDA, Evans PR & McMahon HT (1998) Crystal structure of the amphiphysin-2 SH3 domain and its role in the prevention of dynamin ring formation. *EMBO J* 17: 5273–5285

Peter BJ, Kent HM, Mills IG, Vallis Y, Butler PJG, Evans PR & McMahon HT (2004) BAR Domains as Sensors of Membrane Curvature: The Amphiphysin BAR Structure. *Science (80-)* 303: 495–499

Pineda-Lucena A, Ho CSW, Mao DYL, Sheng Y, Laister RC, Muhandiram R, Lu Y, Seet BT, Katz S, Szyperski T, *et al* (2005) A structure-based model of the c-Myc/Bin1

protein interaction shows alternative splicing of Bin1 and c-Myc phosphorylation are key binding determinants. *J Mol Biol* 351: 182–194

Prokic I, Cowling BS & Laporte J (2014) Amphiphysin 2 (BIN1) in physiology and diseases. *J Mol Med* 92: 453–463

Ramjaun AR & McPherson PS (1998) Multiple amphiphysin II splice variants display differential clathrin binding: Identification of two distinct clathrin-binding sites. *J Neurochem* 70: 2369–2376

Razzaq A, Robinson IM, McMahon HT, Skepper JN, Su Y, Zelhof AC, Jackson AP, Gay NJ & O'Kane CJ (2001) Amphiphysin is necessary for organization of the excitation-contraction coupling machinery of muscles, but not for synaptic vesicle endocytosis in Drosophila. *Genes Dev* 15: 2967–2979

Sahni N, Yi S, Taipale M, Fuxman Bass JI, Coulombe-Huntington J, Yang F, Peng J, Weile J, Karras GI, Wang Y, *et al* (2015) Widespread macromolecular interaction perturbations in human genetic disorders. *Cell* 161: 647–660

Sherry ST, Ward MH, Kholodov M, Baker J, Phan L, Smigielski EM & Sirotkin K (2001) dbSNP: The NCBI database of genetic variation. *Nucleic Acids Res* 29: 308–311

Tossavainen H, Aitio O, Hellman M, Saksela K & Permi P (2016) Structural basis of the high affinity interaction between the Alphavirus nonstructural protein-3 (nsP3) and the SH3 domain of amphiphysin-2. *J Biol Chem* 291: 16307–16317

Tunyasuvunakool K, Adler J, Wu Z, Green T, Zielinski M, Žídek A, Bridgland A, Cowie A, Meyer C, Laydon A, *et al* (2021) Highly accurate protein structure prediction for the human proteome. *Nature* 596: 590–596

Vincentelli R, Luck K, Poirson J, Polanowska J, Abdat J, Blémont M, Turchetto J, Iv F, Ricquier K, Straub M-L, *et al* (2015) Quantifying domain-ligand affinities and specificities by high-throughput holdup assay. *Nat Methods* 12: 787–93

Volchuk A, Narine S, Foster LJ, Grabs D, De Camilli P & Klip A (1998) Perturbation of dynamin II with an amphiphysin SH3 domain increases GLUT4 glucose transporters at the plasma membrane in 3T3-L1 adipocytes. Dynamin II participates in GLUT4 endocytosis. *J Biol Chem* 273: 8169–8176

Wu C, Ma MH, Brown KR, Geisler M, Li L, Tzeng E, Jia CYH, Jurisica I & Li SSC (2007) Systematic identification of SH3 domain-mediated human protein-protein interactions by peptide array target screening. *Proteomics* 7: 1775–1785

Wu T & Baumgart T (2014) BIN1 membrane curvature sensing and generation show autoinhibition regulated by downstream ligands and PI(4,5)P2. *Biochemistry* 53: 7297–7309

Zambo B, Morlet B, Negroni L, Trave G & Gogl G (2022) Native holdup (nHU) to measure binding affinities from cell extracts. *Sci Adv* 8: eade3828

Zanoteli E, Oliveira ASB, Gabbai AA, Laporte J, Kretz C, Mandel JL, Buj-Bello A, Rocha JCC & Perez ABA (2005) Deletion of both MTM1 and MTMR1 genes in a boy with myotubular myopathy [2]. *Am J Med Genet* 134 A: 338–340

Main Figures

Figure 1, Involvement of BIN1 in membrane remodeling and a compendium of known BIN1 interaction partners. (A) Models of vesicle and T-tubule formation in the context of BIN1 and DNM2. BIN1 interplays in both processes, through its membrane-bending/tubulating BAR domain and its SH3 domain. In clathrin-, or caveolin-coated vesicle formation, as well as during the formation of recycling endosomes, the recruitment of DNM2 by BIN1 is critical for vesicle scission. During T-tubule formation, DNM2 is also recruited, but in this case no scission occurs. (B) Schematic illustration of binding of PRMs to SH3 domains. Due to the 2-fold pseudo-symmetry of PPII helices, class 1 and class 2 PxxP motifs bind in different orientations to SH3 domains (Lim *et al*, 1994). (C) Known interaction partners of full-length BIN1 identified by high-throughput qualitative interactomic studies and the experimental overlap between the different sources (Ellis *et al*, 2012) (Luck *et al*, 2020) (Huttlin *et al*, 2021) (Cho *et al*, 2022). Note that the known SH3-domain mediated interaction partners, that were studied by low-throughput methods, were only detected on a few occasions (DNM2, MYC, RIN3, marked in orange), or no detected at all (TAU/MAPT, CAVIN4).

Figure 2, Affinity measurements between SH3 domain of BIN1 and full-length proteins using nHU-MS. (A) Results of single point nHU-MS experiments carried out with the SH3 domain of BIN1 and total Jurkat extracts. Interaction partners that show deficiency in abundance above the significance threshold (tan line) are colored in orange in case we could identify putative PRMs in their sequence and blue in case we cannot. (B) Measured depletion values were converted to affinities using the functions indicated below panel A, assuming a simple binding mechanism and 10 μM estimated bait concentration. The number of unique affinity measurements performed and the identified BIN1 interaction partners found in a single experiment/in all measurements are indicated below panel B. (C, D) We also performed nHU-MS experiments with a set of closely or a distantly related SH3 domains and compared their affinity profiles with BIN1. This way, we could quantify that related SH3-domains, for example the one found in AMPH, show similarities in their affinity interactomes, displaying statistically significant correlation between the measured affinity constants. In contrast, unrelated SH3 domains, such as the one found in ABL1, bind targets with dissimilar affinities. A linear fit (grey line) and a 95% confidence band (black line) is shown on all affinity comparisons. The statistical significance of correlation was determined by two-tailed, unpaired T-test. See Supplementary Figure 1 and Supplementary Table 1 for further details.

Figure 3, Affinity measurements between SH3 domain of BIN1 and full-length proteins using nHU-MS. (A) Affinity ranking of the 206 full-length interaction partners of the BIN1 SH3 domain. Interaction partners found in previous studies, as well as partners whose importance was found to be significant in neuromuscular disorders are indicated. (B) A titration nHU-WB experiment was used to further characterize the interaction between BIN1 and DNM2, directly from a total myoblast extract. A strong interaction was obtained with an apparent partial activity of 76%. (C) A titration holdup experiment was performed with purified FL DNM2. A strong interaction was observed with nearly identical affinity and partial activity than what was found in the nHU experiment. See Supplementary Figure 2 and 3 and Supplementary Table 1 for further details.

Figure 4, Affinity measurements between SH3 domain of BIN1 and isolated PRM fragments. (A) Affinity profile of BIN1_SH3, measured using fragmentomic holdup, against 448 synthetic PRMs found in full-length interaction partners identified before with nHU-MS.

176 PRMs were found to bind with BIN1 displaying affinities ranging from low micromolar to a few hundreds of micromolar dissociation constants. These motifs were found in 97 proteins, matching at least a single functional binding site for half of the identified full-length interaction partners. (B) The combination of native and fragmentomic holdup reveals biophysical properties of full-length proteins and elementary binding sites. The measured affinities of intact proteins are indicated with colored boxes and site-specific affinities of individual PRMs are indicated with colored spikes, where colors were adjusted to measured steady-state affinities of FL proteins and PRM sites, respectively. Note that the protein schemes are not to scale to the actual protein length, but the approximate relative positions of indicated PRMs are. (C) Affinity-weighted specificity logo of the SH3 domains of BIN1, AMPH, and ABL1. BIN1 and AMPH nearly uniquely interacts with class 2 PxxP motifs, while ABL1 prefers to bind class 1 PxxP motifs. See Supplementary Figure 4 and 5 and Supplementary Table 2 for further details.

Figure 5, Natural variants of BIN1 can cause affinity perturbation at an interactomic scale. (A) A summary of our affinity interactomic tests performed with 9 natural variants of the BIN1 SH3 domain. Variants colored green have minor effect on affinity interactomes, while variants colored in purple have large impacts on the biophysical properties or the BIN1 SH3 domain. The cumulative Euclidean affinity distances to the WT BIN1, calculated based on the explored 448 dimensional affinity space, are indicated for each variant. For affinities where no detectable binding was observed the detection threshold was used for calculation, hence only the lower limit of the Euclidean distance could be estimated. (B) Location of the assayed variations on the structure of WT BIN1. D537 and Y531 are positioned near the PRM binding interface, F584 is buried in the hydrophobic core of the SH3 domain. The structure of the BIN1 SH3 domain bound to a high affinity peptide taken from SMCHD1 was generated using AlphaFold2 (Tunyasuvunakool *et al*, 2021). (C) Affinity interactome profiles of the BIN1 variants (colored in green or purple) compared with the affinity profile of WT BIN1 (colored in black). Motifs in the affinity profiles were ranked according to their affinities measured with WT BIN1. Only the motifs displaying detectable binding out of the 449 assayed PRMs are shown. See Supplementary Figure 5 and Supplementary Table 2 for further details.

Figure 6, Natural BIN1 variants of unknown clinical significance may be important in neuromuscular disorders. (A) Affinity profile of the PRR of DNM2 comprising multiple PRM repeats against a set of natural BIN1 variants. Most variants interact with DNM2 with similar affinities, but Y531S, D537V and F584S variations apparently disrupt this interaction. (B) Membrane tubulation assay performed with WT BIN1 and DNM2, as well as Q540H variant which have a minor impact on the affinity interactome of the SH3 domain. (C) Membrane tubulation assay performed with the variants displaying perturbed interactomes. Cos-1 cells were transfected with GFP-BIN1 and Myc-DNM2. While the interactomic impact of F584S seems to be rescued in the context of FL BIN1, both Y531S and D537V variants are unable to recruit full-length DNM2 in cells to membrane tubules. See Supplementary Figure 6 for additional images.

Material and Methods

Cloning and Protein Expression, Purification

SH3 domain coding sequences (BIN1, UniProt ID O00499, residues 513-593; AMPH, UniProt ID P49418, residues 615-695; PRMT2, UniProt ID P55345, residues 24-96; OBSCN, UniProt ID Q5VST9, residues 5594-5674; ARHGEF7, UniProt ID Q14155, residues 178-251; ABL1, UniProt ID P00519, residues 56-121) were obtained from cDNA pools using standard protocols. For nHU and fragmetnomic holdup reactions, SH3 domains were cloned as His_6-AviTag-MBP-TEV-SH3, or His_6-MBP-TEV-SH3 constructs in custom pET vectors, respectively. The empty His_6-AviTag-MBP-TEV-STOP vector was used to produce biotinylated MBP for nHU control experiments. BIN1 variants were created with standard QuickChange strategy.

Biotinylated proteins were co-expressed with BirA (PET21a-BirA, Addgene #20857) in *E. coli* BL21(DE3) cells. At Isopropyl β-D-1-thiogalactopyranoside (IPTG) induction (1 mM IPTG at 18 ºC for ON), 50 µM biotin was added to the media. Harvested cells were lysed in a buffer containing 50 mM TRIS pH 7.5, 150-300 mM NaCl, 50 µM biotin, 2 mM 2-mercaptoethanol (BME), cOmplete EDTA-free protease inhibitor cocktail (Roche, Basel, Switzerland), 1% Triton X-100, and trace amount of DNAse, RNAse, and Lysozyme. Lysates were frozen at -20 ºC before further purification steps. Lysates were sonicated and centrifuged for clarification. Expressed proteins were captured on pre-packed Ni-IDA (Protino Ni-IDA Resin, Macherey-Nagel, Duren, Germany) columns, were washed with at least 10 column volume cold wash buffer (50 mM TRIS pH 7.5, 150 mM NaCl, 2 mM BME) before elution with 250 mM imidazole. The Ni-elution was collected directly on a pre-equilibrated amylose column (amylose high flow resin, New England Biolabs, Ipswich, Massachusetts). Amylose column was washed with 5 column volume cold wash buffer before fractionated elution in a buffer containing 25 mM Hepes pH 7.5, 150 mM NaCl, 1 mM TCEP, 10% glycerol, 5 mM maltose, cOmplete EDTA-free protease inhibitor cocktail. The concentration of proteins was determined by their UV absorption at 280 nm before aliquots were snap frozen in liquid nitrogen and were stored at -80 ºC. Non-biotinylated proteins were produced identically but without co-transformation with BirA and without supplementing the media or the lysis buffer with biotin.

Purification and enzymatic characterization of FL DNM2

Human DNM2 protein was produced from pVL1392 plasmid in Sf9 cells with the baculovirus system as described previously (Lionello *et al*, 2022). Briefly, a transfection was performed with the DNM2 plasmid to produce viruses. Sf9 cells were infected with viruses and grown for 3 d at 27°C and then centrifuged at 2,000 x g for 10 min. DNM2 recombinant protein was resuspended in buffer A (20 mM HEPES, pH 7,4; 150 mM NaCl, 5 % of Glycerol, 1 mM EGTA, 1 mM DTT) and purified with GST-BIN1_SH3 bound to Glutathione-Sepharose 4B beads (GE Healthcare). Human SH3 of BIN1 with GST tag (GST-SH3) was produced from pGEX6P1 plasmid in *Escherichia coli* BL21. *E. coli* producing this recombinant protein were induced with 1 mM IPTG for 3 h at 37°C, centrifuged at 7,500 x g, and the protein was purified using Glutathione Sepharose 4B beads (GSH-resin). The BIN1_SH3-bound DNM2 was eluted with buffer B (20 mM PIPES, pH 6,8; 1200 mM NaCl). After elution, the pooled elution fractions were dialyzed with buffer A.

GTPase activity of recombinant DNM2 was measured with malachite green assay as previously described with a reaction time of 10, 30 or 180 minutes at 37°C (Gómez-Oca *et al*, 2022). DNM2 recombinant protein was incubated with 2-Diacyl-sn-glycero-3-phospho-L-serine (PS, 4 µg/ml) and 30 mM of NaCl. The concentration of GTP in the

reaction mix was 0.3 mM. The tested concentrations of DNM2 recombinant protein were from 2 to 64 nM.

Peptide synthesis

The DNM2 PRR peptide (residues 823-860) was chemically synthesized on an ABI 443A synthesizer with standard Fmoc strategy with biotin group attached to the N-terminus via a TTDS (Trioxatridecan-succinamic acid) linker and was HPLC purified (>95% purity). Predicted peptide mass was confirmed by MS and peptide concentration was determined based on dry weight.

The PxxP peptide library was prepared as described in details before (Gogl *et al*, 2022). Briefly, peptides were synthetized with standard Fmoc strategy in 96-well plate format using an Intavis multipep Rsi. Peptides were amidated C-terminally and were N-terminally tagged with biotin via an Ado-Ado (amino-dodecanoic acid), or a Glu-Glu-Ado-Ado linker. Predicted peptide masses were confirmed by MS and average peptide concentrations were determined based on the excess weight of the entire 96-well plate after drying and were used in 10-50× molar excess during the holdup experiments.

Mammalian cell extract preparation

Jurkat E6.1 cells (ECACC #88042803, RRID: CVCL_0367) were grown in RPMI (Gibco) medium completed with 10% FBS (Gibco BRL) and 40 µg/ml gentamicin (Gibco/Life Technology). The C25 myoblast cell line obtained from Institut de Myologie (Paris, France) were grown below 60% confluency in DMEM/199 medium (Sigma-Aldrich) supplemented with 20% FBS, 25 µg/ml fetuin (Sigma-Aldrich), 0.5 ng/ml basic fibroblast growth factor (Gibco BRL), 5 ng/ml epidermal growth factor (Gibco BRL), 0.2 µg/ml dexamethasone (Sigma-Aldrich), 5 µg/ml insulin (Eli Lilly Co., Indianapolis, USA), 50 U/ml penicillin (Gibco/ Life Technology), and 100 µg/ml gentamicin. All cells were kept at 37°C and 5% CO_2. To prepare total cell extracts, Jurkat cells were seeded onto T-175 flasks and grew until $3x10^6$ cells/ml confluency, C25 myoblasts were seeded on T-75 flasks and grew until they reach ½ confluency, where we detected the highest expression for DNM2 in these cells before. Jurkat cells were collected by 1,000 g x 5 min centrifugation, washed with PBS and then lysed in ice-cold lysis buffer (Hepes-KOH pH 7.5 50 mM, NaCl 150 mM, Triton X-100 1%, cOmplete EDTA-free protease inhibitor cocktail 5x, EDTA 2 mM, TCEP 5 mM, glycerol 10%). C25 myoblasts were lysed with the same lysis buffer directly on the flasks after washing them with PBS, and the cells were collected by scraping. Lysates were sonicated 4x20 sec with 1 sec long pulses on ice, then incubated rotating at 4°C for 30 min. The lysates were centrifuged at 12,000 rpm 4°C for 20 min and supernatant was kept. Total protein concentration was measured by standard Bradford method (Bio-Rad Protein Assay Dye Reagent #5000006) using a BSA calibration curve (MP Biomedicals #160069, diluted in lysis buffer) on a Bio-Rad SmartSpec 3000 spectrophotometer instrument. Lysates were diluted to 2 mg/ml concentration, aliquoted and snap-frozen in liquid nitrogen and stored at -80°C until measurement.

Single-point nHU experiment

For single-point nHU experiments carried out at ~10 µM estimated bait concentration, pre-equilibrated 25 µl streptavidin resin (Streptavidin Sepharose High Performance, Cytiva) was incubated with 1 ml 25-40 µM purified biotinylated MBP or MBP-fused SH3 domains for 1 hour at room temperature. After the incubation, all resins were washed with 20 resin volume (500 µl) holdup buffer (50 mM Tris pH 7.5, 300 mM NaCl, 1 mM TCEP, .22 filtered). The washed resins were then mixed with 25 µl 1 mM biotin solution, diluted in 10 resin volume holdup buffer and were incubated for 10 minutes at room temperature. Then, the resulting resins were washed three more times with 20 resin volume holdup buffer. The

resulting SH3-saturated resins were mixed with 100 µl 2 mg/ml Jurkat extracts and were incubated at 4 ºC for 2 h with constant mild agitation. After the incubation ended, the solid and liquid phases were separated by a brief centrifugation (15 sec, 2000 g) and 70 µl of the supernatant was recovered rapidly. Then, to minimize carryover contamination from resin, the recovered supernatants were centrifuged one more time and 50 µl of the supernatant was recovered that was subjected for mass spectrometry analysis. As described in details before, measurements were done in singlicates against duplicate controls with injection triplicates during MS measurements (Zambo *et al*, 2022). The experiment series carried out with the 6 SH3 domains was analyzed on the Orbitrap Exploris 480 MS and the measurement with BIN1_SH3 alone was analyzed with Orbitrap Elite.

MS analysis was performed as described in details before (Zambo *et al*, 2022). Briefly, nHU samples were precipitated with TCA, and the urea-solubilized, reduced and alkylated proteins were digested with trypsin and Lys-C at 2M final urea concentration. Peptide mixtures were then desalted on C18 spin-column and dried on Speed-Vacuum. 100 ng peptide mixtures were analyzed using an Ultimate 3000 nano-RSLC coupled in line, via a nano-electrospray ionization source, with a LTQ-Orbitrap ELITE mass spectrometer (Thermo Fisher Scientific, San Jose, California) or with the Orbitrap Exploris 480 mass-spectrometer (Thermo Fisher Scientific, Bremen, Germany) equipped with a FAIMS (high Field Asymmetric Ion Mobility Spectrometry) module. Data was collected in DDA (data dependent acquisition) mode, proteins were identified by database searching using SequestHT (Thermo Fisher Scientific) with Proteome Discoverer software (Thermo Fisher Scientific). Peptides and proteins were filtered with a false discovery rate (FDR) at 1%. Label-free quantification was based on the extracted ion chromatography intensity of the peptides. All samples were measured in technical triplicates. The measured extracted ion chromatogram (XIC) intensities were normalized based on median intensities of the entire dataset to correct minor loading differences. For statistical tests and enrichment calculations, not detectable intensity values were treated with an imputation method, where the missing values were replaced by random values similar to the 10% of the lowest intensity values present in the entire dataset. Unpaired two tailed T-test, assuming equal variance, were performed on obtained $\log_2$ XIC intensities. All raw LC-MS/MS data have been deposited to the ProteomeXchange via the PRIDE database with identifier 1-20230214-20023.

Obtained fold-change values were converted to apparent affinities using the hyperbolic binding equation and binding thresholds were determined as described before (Zambo *et al*, 2022). Proteins containing PRMs were identified with the help of SliMSearch using the class 1 and class 2 PxxP consensus motif definitions found in the ELM database (LIG_SH3_1 and LIG_SH3_2) (Krystkowiak & Davey, 2017) (Kumar *et al*, 2019).

Titration nHU and HU experiments

Titration holdup experiments were carried out as described above using 25 µl saturated resins prepared (Zambo *et al*, 2022). Briefly, we mixed MBP, or BIN1_SH3 saturated resins and certain proportions and kept the total resin-analyte ratio constant during the experiment (for 25 µl we used 100 µl analyte). Experiments were carried out at 4 ºC for 2 h and recovered supernatants were subjected to Western blot. As analyte, either total myoblast extracts (2 mg/ml) were used in the case of titration nHU experiments, or 62 nM purified DNM2 in the case of titration HU experiments.

Samples were mixed with 4x Laemmli buffer (120 mM Tris-HCl pH 7, 8% SDS, 100 mM DTT, 32% glycerol, 0.004% bromphenol blue, 1% β-mercaptoethanol) in 3:1 ratio.

Equal amounts of samples were loaded on 10% acrylamide-gels. Transfer was done into PVDF membranes using a Trans-Blot Turbo Transfer System and Trans-Blot Turbo RTA Transfer Kit (BioRad, #1704273). After 1 hour of blocking in 5% milk, membranes were incubated overnight 4°C in primary DNM2 antibody (in-house antibody #2641, rabbit polyclonal, IGBMC) in 5% milk. Membranes were washed three times with TBS-Tween and incubated at RT for 1 h in secondary antibody (goat anti-rabbit(H+L) #111-035-003 RRID: AB_2313567) in 5% milk (dilution: 1:10,000). After washing three times with TBS-Tween, membranes were exposed to chemiluminescent HRP substrate (Immobilon, #WBKLS0100) and captured in docking system (Amersham Imager 600, GE). Then, membranes were exposed to 15% H_2O_2 to remove secondary signal and the membranes were incubated with anti-GAPDH primary antibody (1:5000, Sigma #MAB374, clone 6C5, RRID: AB_2107445) for 1 hour at room temperature. After three washings, the membranes were incubated with the secondary antibody (goat anti-mouse(H+L) #115-035-146 RRID: AB_2307392) in 5% milk (concentration 1:10,000), washed three times and captured in the docking system as above. Densitometry was carried out on raw Tif images by using Fiji ImageJ 1.53c.

As mentioned before, apparent partial binding can occur for many reasons, most importantly as a result of heterogeneous intrinsic affinities of the heterogeneous prey, e.g. caused by abundant phosphorylation or oligomerization, or due to technical reasons, e.g. caused by bait leakage from the solid phase or contamination of the recovered supernatant with resin. Unfortunately, both kinds of phenomena results in measured BI values that decrease in the same manner following the formula

$$BI_{ideal} = \frac{BI_{measured}}{f} \quad , \qquad (1)$$

where the *f* factor is either the “fraction of binding capable prey” or the “fraction of resin immobilized bait”. Regardless of the nature of its source, this phenomenon explains why DNM2 appeared as a weaker interaction partner of BIN1 in the single-point nHU assay than in the nHU titration experiment, since affinity calculation was made using a simple binding model that assumed complete binding. To correct affinity measurements taking into consideration such effects, a correction formula could be applied,

$$\Delta K_{app} = \frac{c_{bait} - c_{bait} * f}{BI_{measured}} \quad . \qquad (2)$$

Although it would be possible to correct for such effect systematically, prey partial activity should be decided for every single prey, and resin leakage, where the value of *f* is constant for all preys, is also could be highly difficult to precisely quantify. Thus, we decided to not to apply such correction in the case of single point nHU experiments. In the case of DNM2, since nearly identical partial binding activity was obtained for purified or for endogenous prey, it is unlikely that this phenomenon purely originates from compositional or conformational heterogeneity and it is more likely that the observed partial binding activity originates from at least part from resin leakage, that we indeed observed during the experiment carried out with purified DNM2 .

In order to investigate the origin of the apparent partial activity of the resulting experiments, we also stained the supernatants of the HU titration experiment on 8% acrylamide-gel with Zinc-Imidazole and with colloidal Coomassie (Figure S2). From this experiment, we roughly estimated that approximately 0.5-1 μM amount of immobilized

baits (MBP or MBP-fused BIN1_SH3) leaked to the liquid fraction, accounting for 5-10% of the complete bait amount. This alone could cause an apparent partial activity of 95-90%, yet we observed an apparent partial activity of 77% during analysis. Therefore, we assume that the apparent partial activity is a result of multiple factors, including both technical and biological origins. In the past, we also detected leaking baits in the MS measurements, however the fraction of leaking bait was impossible to accurately determine because substantial carryover contamination was found from recurring abundant tryptic peptides of MBP on our chromatographic system. Although we could apply a correction for this bait leakage in the nHU-MS experiments (5-10%, according to the quantified amounts based on protein staining), we decided not to do because it would lead to unrealistic BI values (above 1) for several measurements. Similarly, we obtained (near) complete binding in previous nHU experiments and therefore it is unlikely that such correction would be necessary to perform with every experiment systematically.

Fragmentomic holdup assay

Fragmentomic holdup assays were carried out in 384 well filter plates using intrinsic fluorescence as a readout following the exact same protocol that was described in details before (Gogl *et al*, 2022). Briefly, 5 µl of streptavidin resin, pre-saturated with peptides, were aliquoted on filter plates and the holdup reaction was carried out with 10 µl analyte in holdup buffer, complemented with 4 µM double-affinity purified MBP-fused SH3 domain, as well as 50 nM fluorescein and 100 nM mCherry as internal standards. Filtrates were analyzed on a PHERAstar (BMG Labtech, Offenburg, Germany) microplate reader by using 485 ± 10 nm–528 ± 10 nm (fluorescein), 575 ± 10 nm–620 ± 10 nm (mCherry), and 295 ± 10 nm–350 ± 10 nm (Trp-fluorescence) band-pass filters. Filter plates with peptide-saturated beads were recycled as before. However, we have found that unlike PDZ-binding motifs, PxxP motifs were difficult to recycle several times and an apparent decrease of bait concentration was often found, which was possible to minimize by long incubations in holdup buffer. We hypothetize that this phenomena is caused by some sort of hydrophobic collapse. Regardless, we decided to only recycle each filter plate only a few times (5-10, while we could safely recycle PDZ-binding motif saturated plates >20 times). When small apparent bait concentration decrease was obtained, we corrected the measured values based on previous measurements. In the case of BIN1 variants that were found to show perturbed interactomes, measurements were repeated on fresh filter plates to eliminate the possibility of disturbing the results (e.g. false negatives or positives). Affinity-weighted specificity logos were calculated as described before (Gogl *et al*, 2022). The obtained affinities (both fragmentomic and of FL proteins obtained from nHU experiments) were uploaded to the ProfAff affinity database and accessible at https://profaff.igbmc.science (Gogl *et al*, 2022).

Membrane tubulation assay

pTL1 myc-His plasmids containing the human DNM2 and pEGFP-BIN1 plasmid (human BIN1 isoform 8) have been previously used (Nicot *et al*, 2007). Mutant versions of BIN1 were created by standard QuickChange mutagenesis protocol.

Cos-1 cells (ATCC #CRL-1650, RRID: CVCL_0223) were grown in DMEM (1g/L glucose) containing 10% FCS and 40 µg/mL gentamicin, kept at 37°C and 5% CO2 and were split twice a week for maintaining. The day before transfection, 0.375 x 10^5 cells were seeded in the wells of a 24-well plate with coverslips. Cells were co-transfected with 0.5 µg of DNM2 and 0.25 µg of BIN1 (either WT or mutants) per well using JetPRIME reagent (Polyplus, #101000046) according to the manufacturer's recommendations. The medium was changed to fresh medium after 5 hours of transfection to enhance survival after transfection.

Immunostaining was carried out after 24 hours of transfection. Cells were washed once with sterile PBS and fixed with 4% formaldehyde solution for 15 minutes at room temperature. After washing three times with PBS, cells were permeabilized with 0.2% Triton X-100 in PBS for 10 minutes. Then, cells were blocked in blocking solution (30 mL PBS, 1.5 g BSA powder (MP Biomedicals #160069), 0.1% Triton X-100) for 1 hour at room temperature. Cells were incubated with the primary antibody anti-myc (Thermo Fisher, clone 9E10, #13-2500, RRID: AB_86583, dilution: 1:500) in blocking solution overnight at 4 °C. The next day, cells were washed three times with PBS and were incubated with secondary antibody Alexa Fluor 594 conjugated anti-mouse (Invitrogen, #A-11032, RRID: AB_2534091, dilution: 1:1,000) in blocking solution for 1 hour at room temperature. Cells were washed again three times with PBS, and coverslips were mounted with DAPI containing Vectashield (#H-1200) on slides. Images were taken using a Leica SP5 confocal microscope (Leica Camera AG, Wetzlar, Germany) with an HCX PL APO 63×/1.40 to 0.60 oil objective using excitation at 405 nm (diode), 488 nm (Argon laser), and 594 nm (HeNe laser) and emission at 415 to 480, 510 to 560, and 610 to 695 nm for DAPI (nucleus), GFP (BIN1), and Alexa 594 (DNM2), respectively. Image analysis was done using Fiji ImageJ 1.53c software.

To determine single cell co-localization of BIN1 variants and DNM2, Pearson correlation coefficients were calculated using Coloc 2 plugin with auto-threshold in ImageJ. In every image, those cells were only selected by ROI, which showed membrane tubules in the green (BIN1) channel and expressed both GFP-BIN1 and DNM2, i.e. there were signal in both green and red channels for the given cell. Statistics were done using GraphPad Prism 7 software.

Supplementary Figures

Supplementary Figure 1, Additional results of nHU-MS experiments. (A-E) Results of single point nHU-MS experiments carried out with the SH3 domains of AMPH, ABL1, ARHGEF7, PRMT2, and OBSCN using total Jurkat extracts (left). Interaction partners that show deficiency in abundance above the significance threshold (tan line) are colored in orange in case we could identify putative class 1/2 PxxP motifs in their sequence and blue in case we cannot. Measured depletion values were converted to affinities using a 10 μM estimated bait concentration assuming simple binding mechanism (middle/right). (C, D, E) On panel C, D and E, an additional comparison is shown with the affinities of BIN1 affinities (extreme right panel). (F) Result of an independent single point nHU-MS experiment carried out with the SH3 domain of BIN1 measured on a different mass spectrometer (Orbitrap Elite). On the right panel a comparison is shown with the independently measured BIN1 affinities, that was analized using an Orbitrap Exploris 480 instrument. A linear fit (grey line) and a 95% confidence band (black line) is shown on all affinity comparisons.

Supplementary Figure 2, Raw results of the titration nHU and titration HU experiments. (A) Titration nHU-WB experiments were carried out using myoblast extracts. The recovered supernatants were assayed using western blot with DNM2 and GAPDH antibodies. (B) Titration HU-WB experiments were carried out using purified DNM2. The recovered supernatants were assayed using western blot with DNM2 antibody. All western blots were repeated 3 times and the measured luminescent signals, overlayed with colorimetric images are shown. (C) Supernatants of the HU-WB experiment were also stained with sensitive protein stains (Zn-Imidalzle and Colloidal Coomassie) to visualize bait leakage.

Supplementary Figure 3, Quality control of purified DNM2. (A) FL human DNM2 was produced in insect cells and was purified on GST column, preloaded with GST-fused BIN1_SH3. DNM2 was eluted at acidic pH and the pooled elution fractions were dialized to a basic pH. (B) Malachite green GTPase activity assay was used to verify the catalytic activity of recombinant DNM2.

Supplementary Figure 4, Site-specific affinity interactomes of other SH3 domains. The affinity interactomes of the five tested SH3 domains are shown (blue) in comparision with the affinity profile of BIN1 (black). Note the highest similarity between the affinity profiles of BIN1 and AMPH. Only the motifs displaying detectable binding are shown. Affinity-weighted specificity logos are shown for PRMT2, ARHGEF7 and OBSCN above their affinity profiles.

Supplementary Figure 5, Quality control of purified MBP-fused SH3 domains used for fragmentomic holdup experiments. The double-affinity purified His_6-MBP-fused SH3 domains were loaded on SDS-PAGE and stained with Coomassie brilliant blue. No major contaminants or degradation products were detected.

Supplementary Figure 6, Additional images of membrane tubulation assay performed with BIN1 variants. Cos-1 cells were transfected with GFP-BIN1 and Myc-DNM2. Confocal images were taken from fixed cells. Rare BIN1 variants Y531S, D537V, and to a lesser degree F584S decreases the amount of DNM2 recruited to BIN1-induced membrane tubules. Below the microscope images, the single-cell co-localization analyzes between the BIN1 variants and DNM2 are shown. P values were calculated between Pearson correlation coefficients (PCC) of WT and missense variants using a two-tailed

unpaired Student's T-test. Box plots indicate the median and upper and lower quartiles, and whiskers label the minimal and maximal measured PCC values. Individual data points representing measurements of single cells are also indicated.

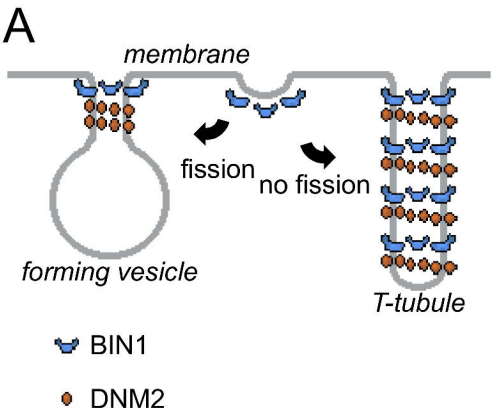
A
membrane
fission
no fission
forming vesicle
T-tubule
BIN1
DNM2

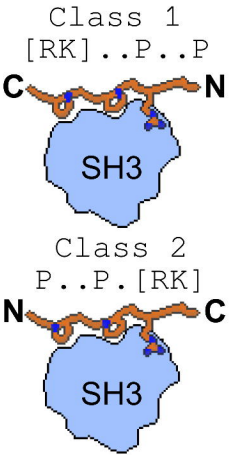
B
Class 1
[RK]..P..P
C
N
SH3
Class 2
P..P.[RK]
N
C
SH3

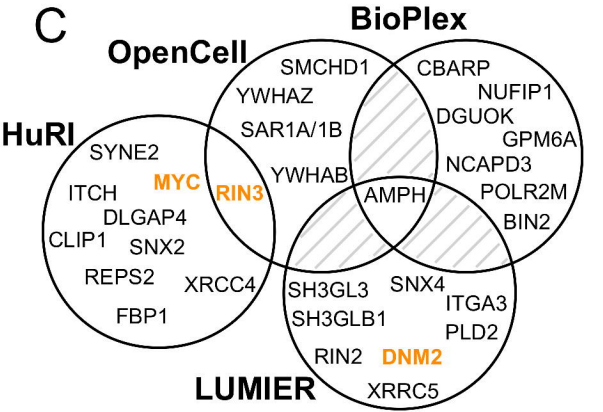
C
BioPlex
OpenCell
HuRI
LUMIER
SMCHD1
YWHAZ
SAR1A/1B
YWHAB
CBARP
NUFIP1
DGUOK
GPM6A
NCAPD3
POLR2M
BIN2
AMPH
SYNE2
ITCH
MYC
RIN3
DLGAP4
CLIP1
SNX2
REPS2
XRCC4
FBP1
SH3GL3
SNX4
ITGA3
SH3GLB1
PLD2
RIN2
DNM2
XRRC5

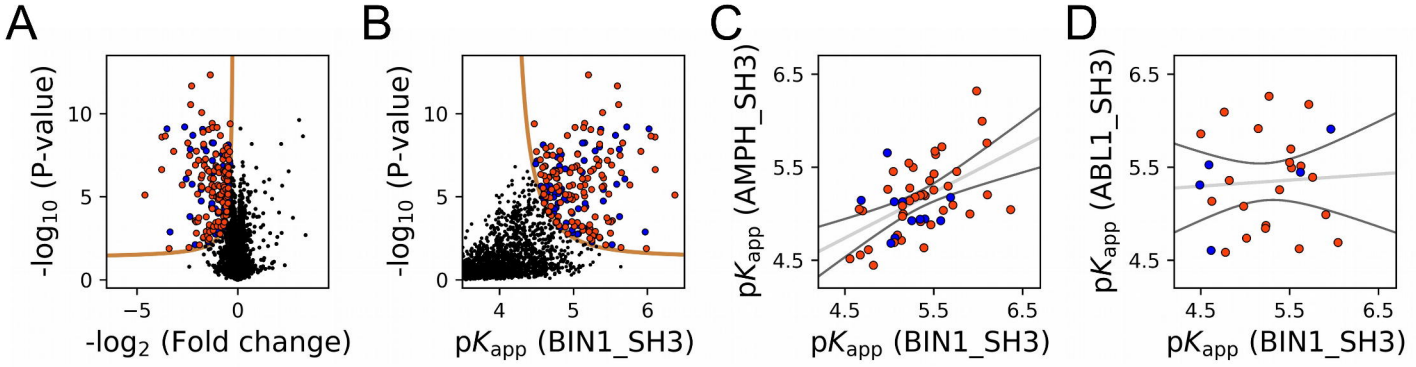
A
B
C
D
-log10 (P-value)
-log2 (Fold change)
pKapp (BIN1_SH3)
pKapp (AMPH_SH3)
pKapp (ABL1_SH3)
Kapp = (Cbait-Cbait*BI)/BI
pKapp = -log10 [Kapp (M)]
Ndetected = 6,357/6,453
Nsignificant binder w/ PRM = 127/133
Nsignificant binder w/o PRM = 61/73
Slope = 0.49
PCC = 0.52
P < 0.001
Slope = 0.07
PCC = 0.06
P = 0.76

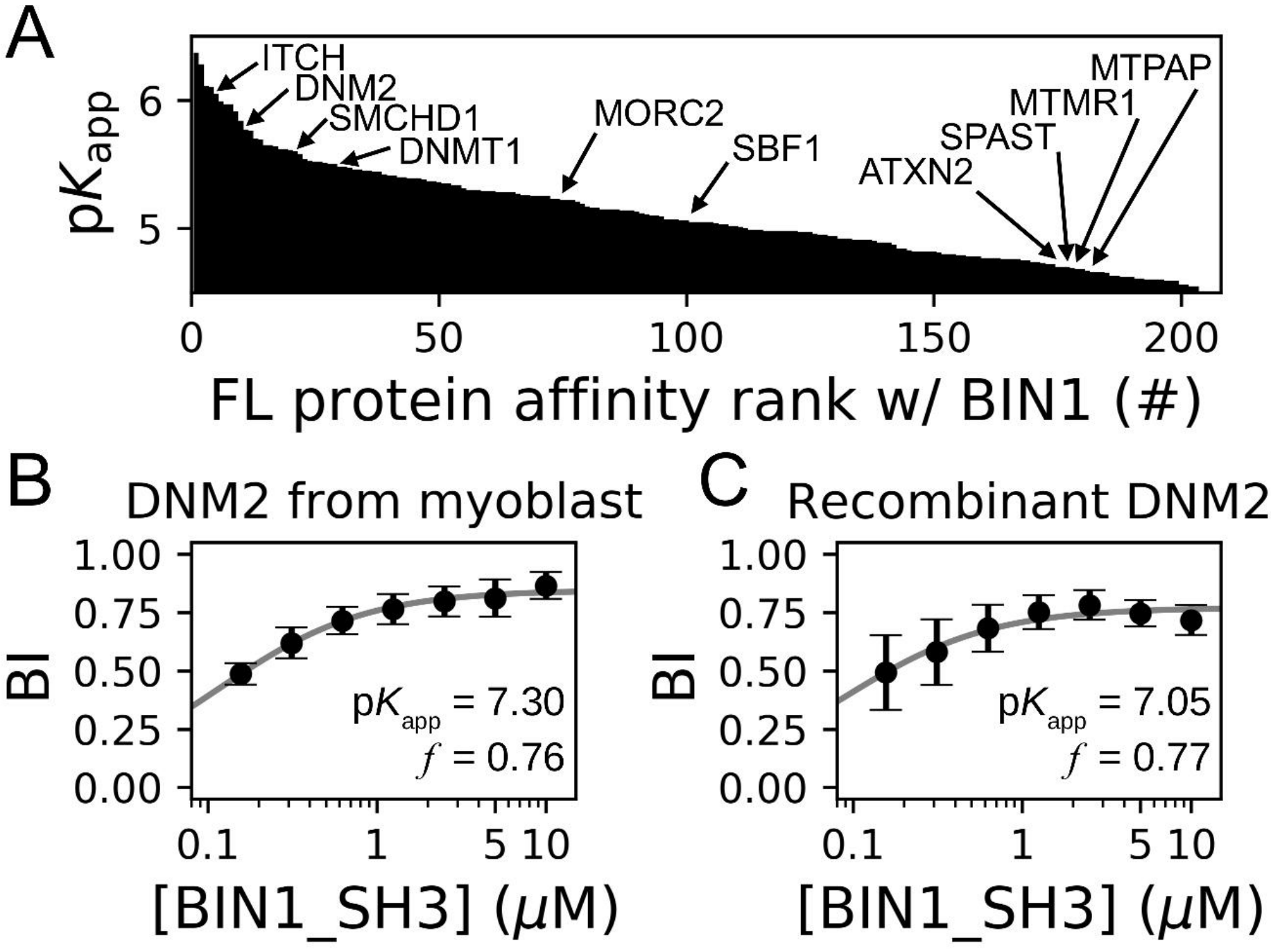
A
ITCH
DNM2
SMCHD1
DNMT1
MORC2
SBF1
ATXN2
SPAST
MTMR1
MTPAP
pKapp
6
5
0
50
100
150
200
FL protein affinity rank w/ BIN1 (#)
B
DNM2 from myoblast
BI
1.00
0.75
0.50
0.25
0.00
pKapp = 7.30
f = 0.76
0.1
1
5 10
[BIN1_SH3] (μM)
C
Recombinant DNM2
BI
1.00
0.75
0.50
0.25
0.00
pKapp = 7.05
f = 0.77
0.1
1
5 10
[BIN1_SH3] (μM)

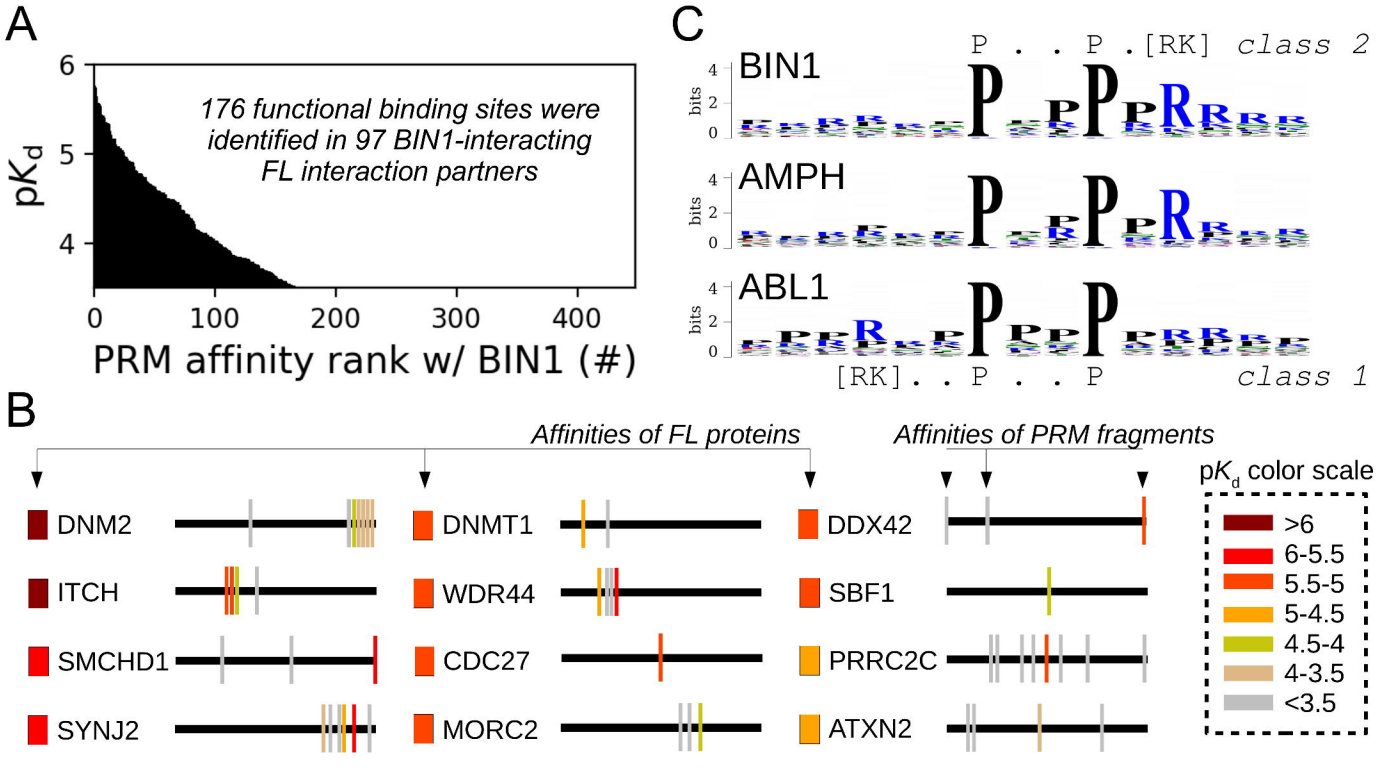
A
176 functional binding sites were identified in 97 BIN1-interacting FL interaction partners
pKd
6
5
4
0
100
200
300
400
PRM affinity rank w/ BIN1 (#)
C
P . . P .[RK] class 2
BIN1
AMPH
ABL1
bits
[RK]. . P . . P class 1
B
Affinities of FL proteins
Affinities of PRM fragments
DNM2
ITCH
SMCHD1
SYNJ2
DNMT1
WDR44
CDC27
MORC2
DDX42
SBF1
PRRC2C
ATXN2
pKd color scale
>6
6-5.5
5.5-5
5-4.5
4.5-4
4-3.5
<3.5

A

Variant	Identifier	Occurance	$\sum_{i=1}^{448} \lvert \Delta pK_{d,i} \rvert \leq$	Interactome
Y531S	rs1455811048	1/251370	93	PAP
T532M	rs112318500	8707/264690	12	Quasi WT
D537V	rs1278822201	2/139050	97	PAP
Q540H	rs561244491	4/251420	23	Quasi WT
P551L	rs1335019359	1/251408	29	Quasi WT
V566M	rs761759946	1/264690	18	Quasi WT
R581C	rs147655157	10/264690	26	Quasi WT
V583I	rs759691190	7/264690	34	Quasi WT
F584S	rs1466748456	1/139050	134	LOF

B

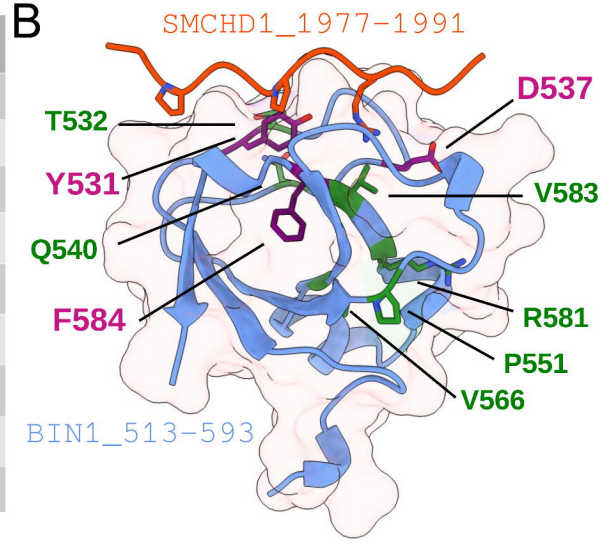

C

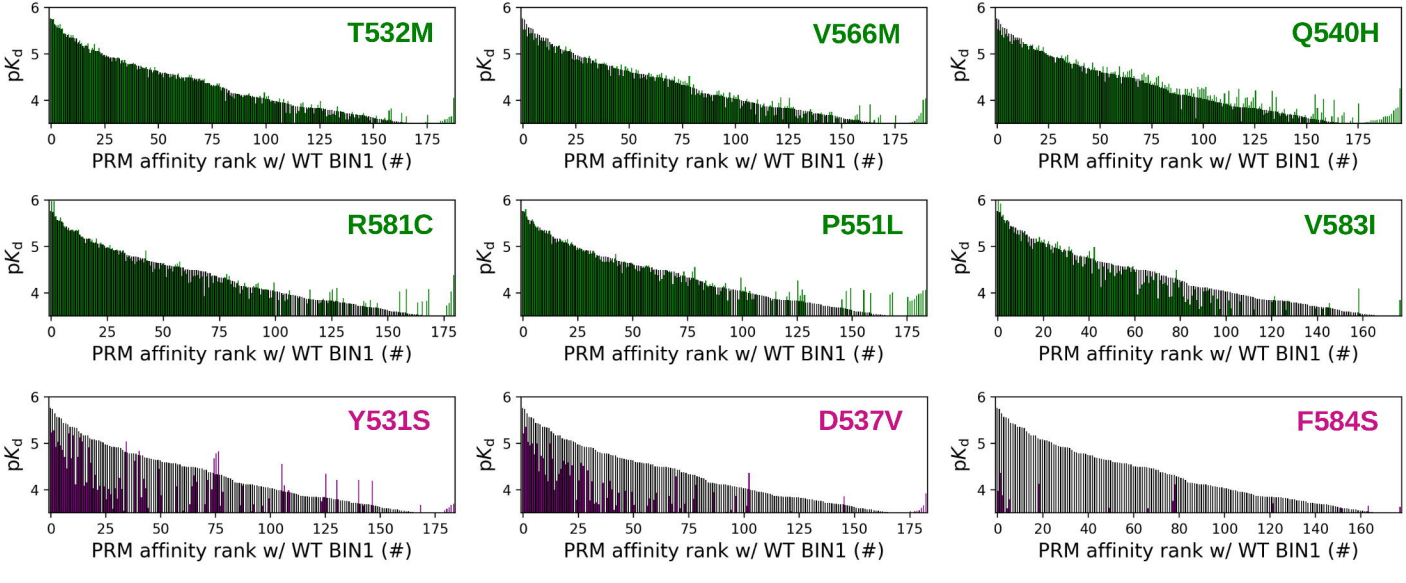

A

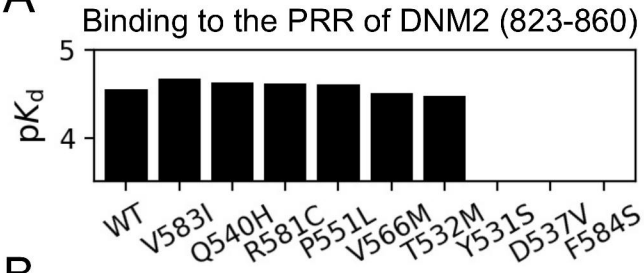
Binding to the PRR of DNM2 (823-860)
pKd
5
4
WT
V583I
Q540H
R581C
P551L
V566M
T532M
Y531S
D537V
F584S

B

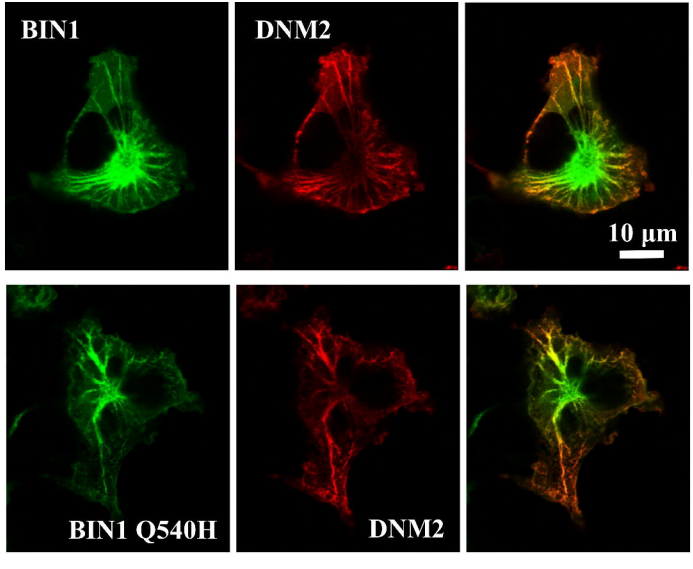
BIN1
DNM2
10 µm
BIN1 Q540H
DNM2

C

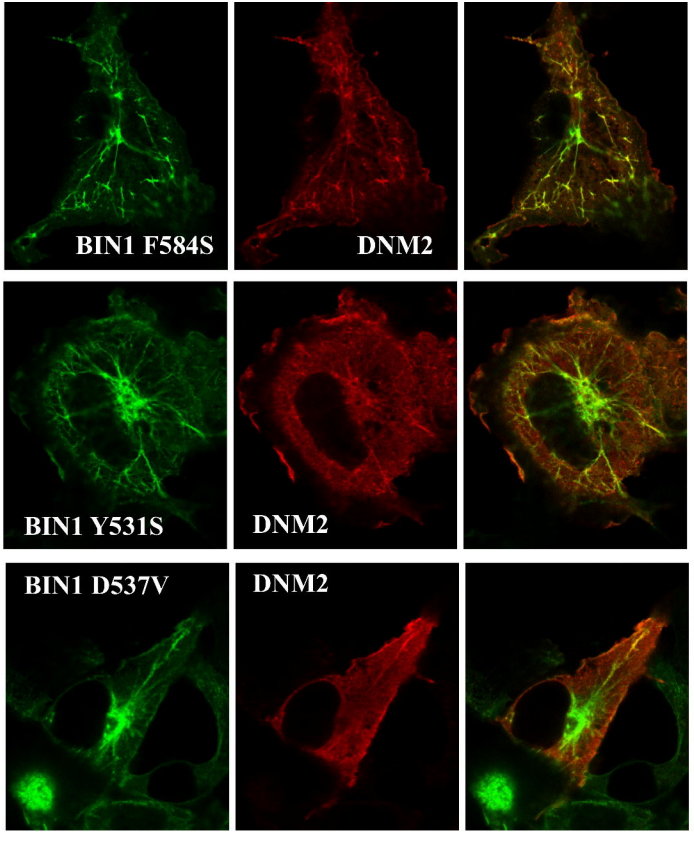
BIN1 F584S
DNM2
BIN1 Y531S
DNM2
BIN1 D537V
DNM2

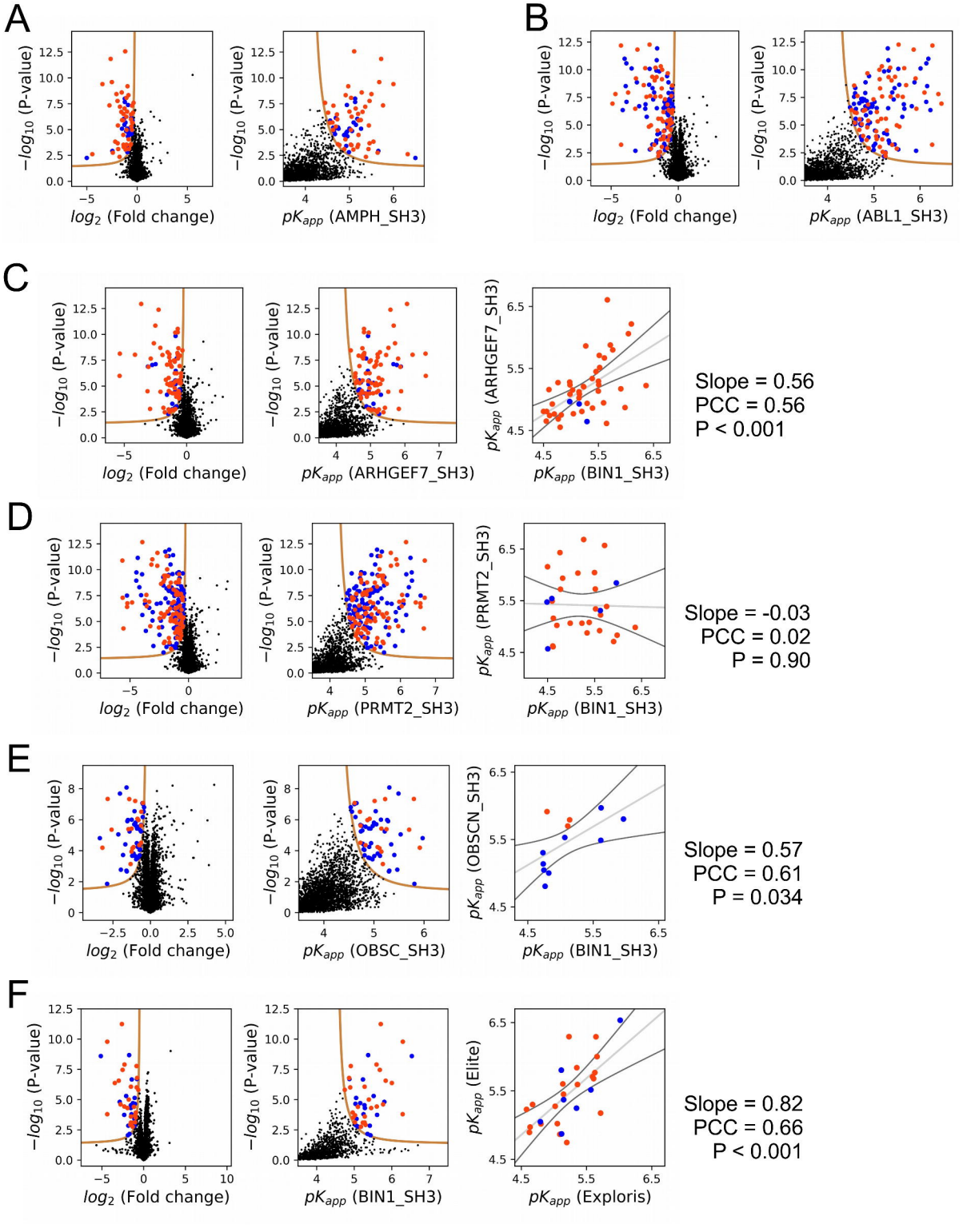
A
B
C
D
E
F
$-log_{10}$ (P-value)
log_2 (Fold change)
pK_{app} (AMPH_SH3)
pK_{app} (ABL1_SH3)
pK_{app} (ARHGEF7_SH3)
pK_{app} (BIN1_SH3)
Slope = 0.56
PCC = 0.56
P < 0.001
pK_{app} (PRMT2_SH3)
Slope = -0.03
PCC = 0.02
P = 0.90
pK_{app} (OBSC_SH3)
pK_{app} (OBSCN_SH3)
Slope = 0.57
PCC = 0.61
P = 0.034
pK_{app} (Elite)
pK_{app} (Exploris)
Slope = 0.82
PCC = 0.66
P < 0.001

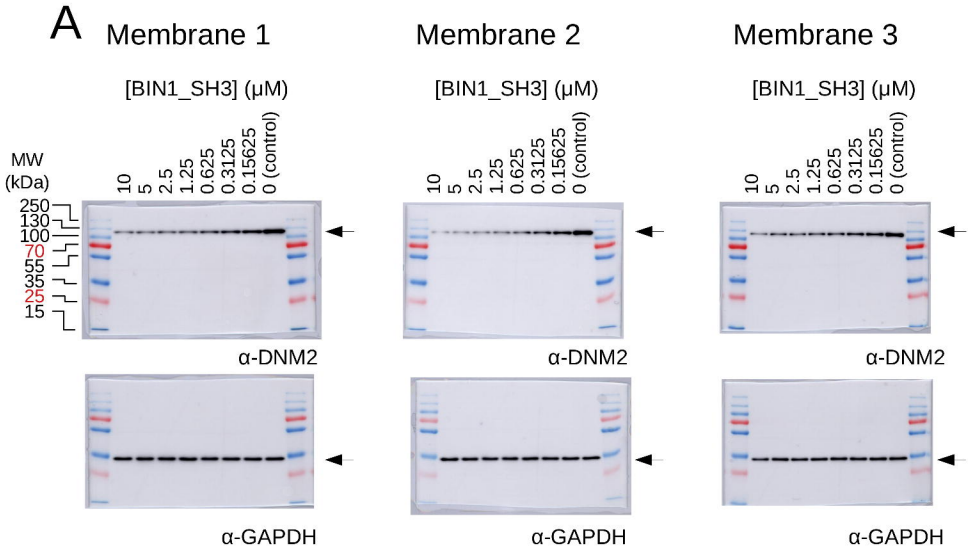

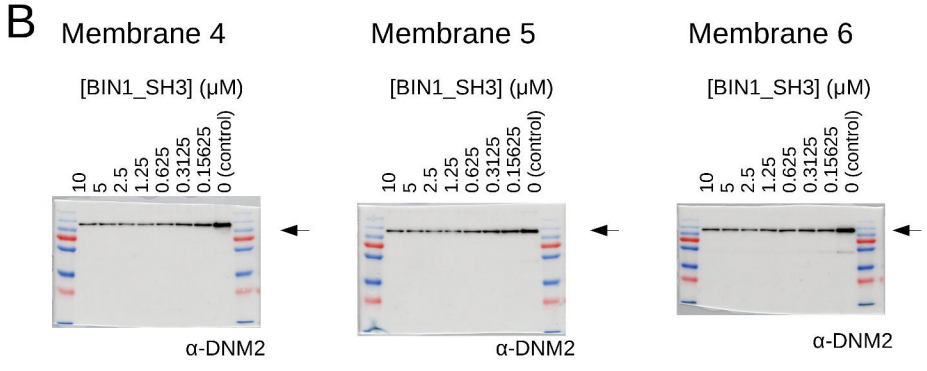

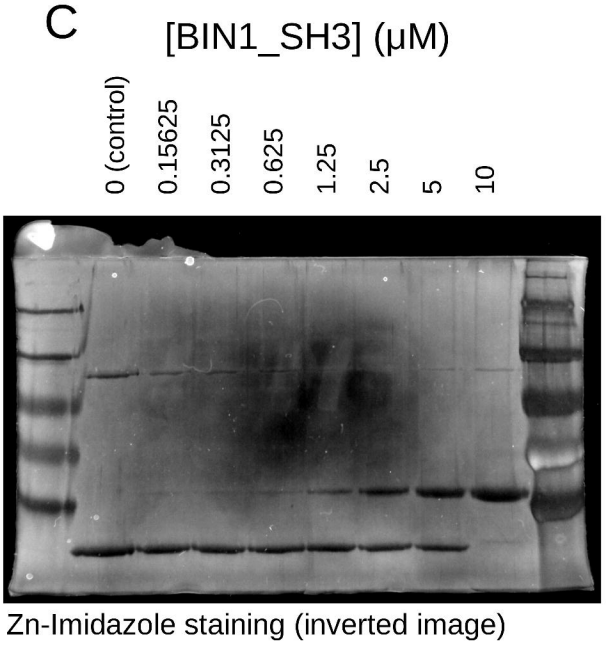

Zn-Imidazole staining (inverted image)

(~50ng DNM2 loaded in control sample)

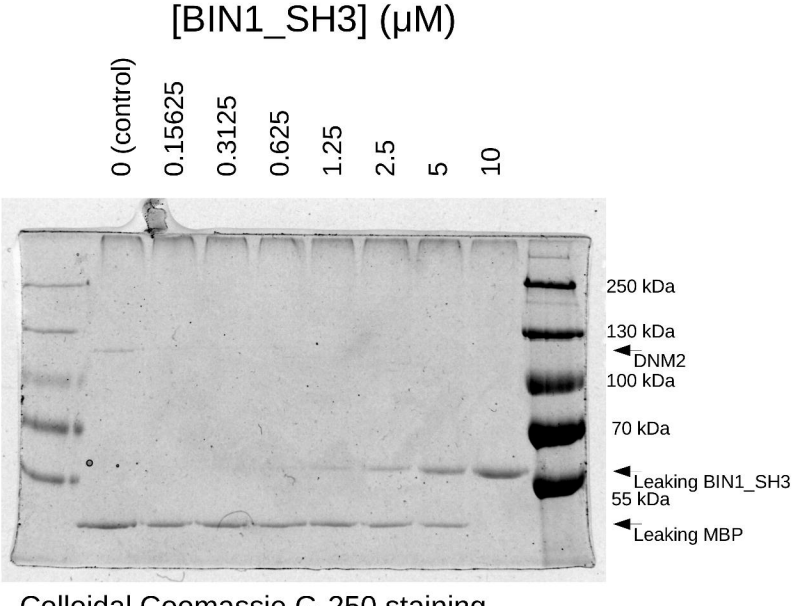

Colloidal Coomassie G-250 staining

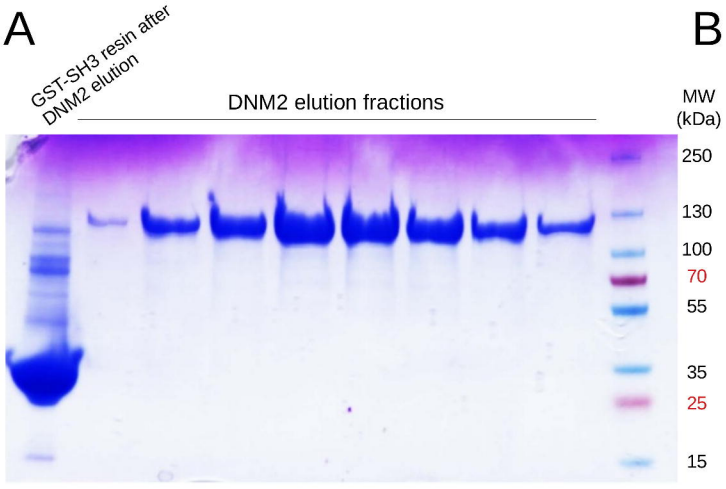
A
GST-SH3 resin after DNM2 elution
DNM2 elution fractions
MW (kDa)
250
130
100
70
55
35
25
15

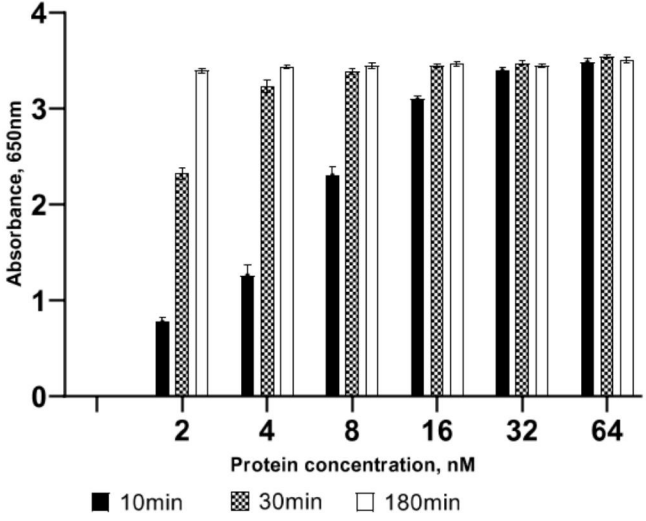
B
Absorbance, 650nm
0
1
2
3
4
2
4
8
16
32
64
Protein concentration, nM
10min
30min
180min

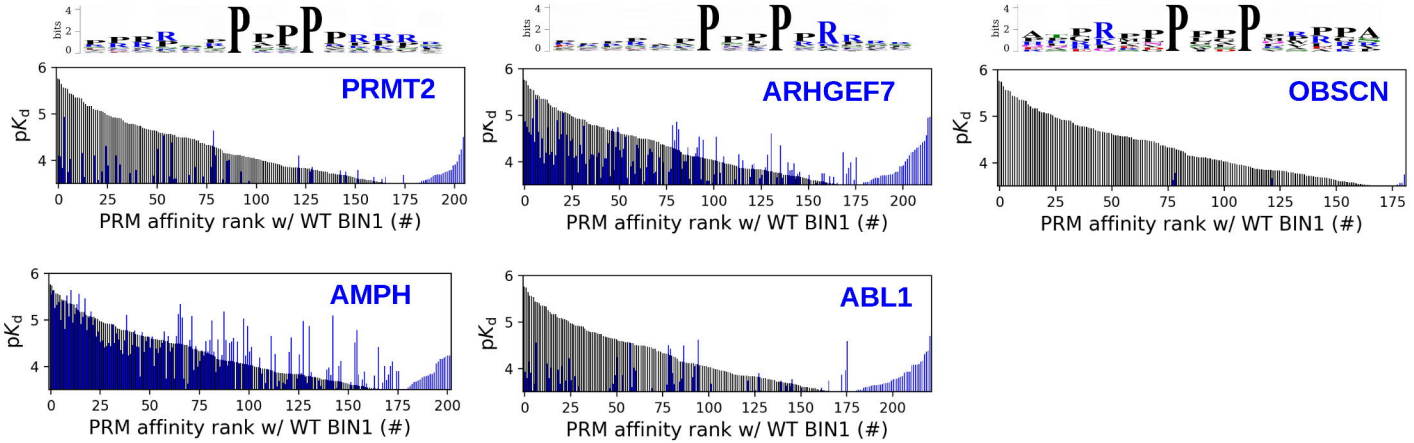
bits
PRMT2
ARHGEF7
OBSCN
AMPH
ABL1
pKd
PRM affinity rank w/ WT BIN1 (#)

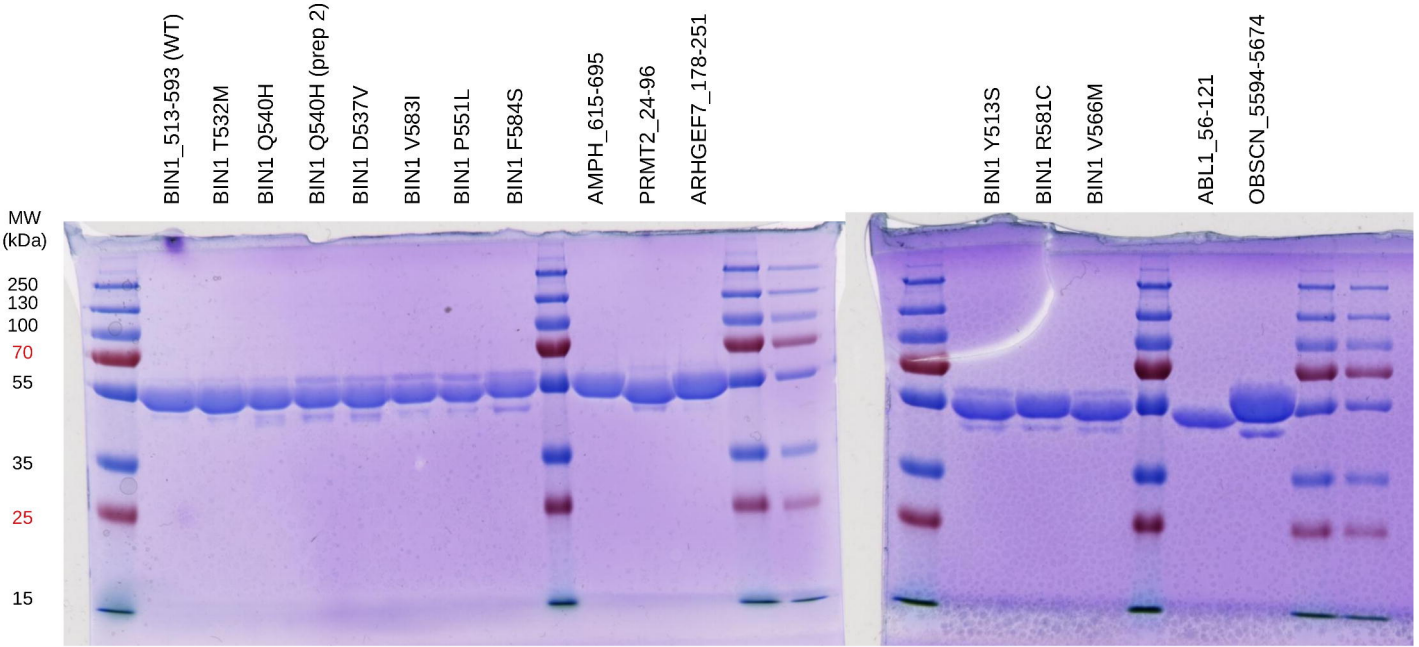
BIN1_513-593 (WT)
BIN1 T532M
BIN1 Q540H
BIN1 Q540H (prep 2)
BIN1 D537V
BIN1 V583I
BIN1 P551L
BIN1 F584S
AMPH_615-695
PRMT2_24-96
ARHGEF7_178-251
BIN1 Y513S
BIN1 R581C
BIN1 V566M
ABL1_56-121
OBSCN_5594-5674
MW
(kDa)
250
130
100
70
55
35
25
15

GFP-BIN1 (WT) Myc-DNM2 Merge GFP-BIN1 (WT) Myc-DNM2 Merge

GFP-BIN1 Q540H Myc-DNM2 Merge GFP-BIN1 Q540H Myc-DNM2 Merge

GFP-BIN1 F584S Myc-DNM2 Merge GFP-BIN1 F584S Myc-DNM2 Merge

GFP-BIN1 Y531S Myc-DNM2 Merge GFP-BIN1 Y531S Myc-DNM2 Merge

GFP-BIN1 D537V Myc-DNM2 Merge GFP-BIN1 D537V Myc-DNM2 Merge
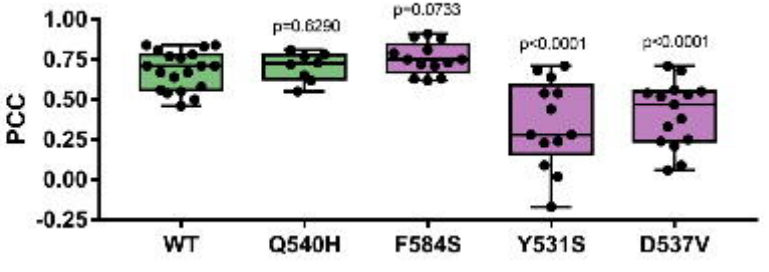
10 μm